AGU PUBLICATIONS

Paleoceanography

RESEARCH ARTICLE
10.1002/2016PA002948

Key Points:
- Reduced-dimension approach facilitates use of Mg/Ca and alkenone proxies, separately and in combination, to reconstruct climate fields
- Single-proxy field reconstructions support cooler SSTs throughout Holocene, but differ in timing and magnitude of maximum anomalies
- Multiproxy field reconstructions support cooler early-Holocene SSTs accompanied by enhanced easterlies compared to present

Correspondence to:
E. C. Gill,
emily.gill@colorado.edu

Citation:
Gill, E. C., B. Rajagopalan, P. Molnar, and T. M. Marchitto (2016), Reduced-dimension reconstruction of the equatorial Pacific SST and zonal wind fields over the past 10,000 years using Mg/Ca and alkenone records, *Paleoceanography*, *31*, 928–952, doi:10.1002/2016PA002948.

Received 8 MAR 2016
Accepted 13 JUN 2016
Accepted article online 20 JUN 2016
Published online 12 JUL 2016

Reduced-dimension reconstruction of the equatorial Pacific SST and zonal wind fields over the past 10,000 years using Mg/Ca and alkenone records

Emily C. Gill[1,2], Balaji Rajagopalan[1,2], Peter Molnar[2,3], and Thomas M. Marchitto[3,4]

[1]Department of Civil, Environmental and Architectural Engineering, University of Colorado Boulder, Boulder, Colorado, USA, [2]Cooperative Institute for Research in Environmental Sciences, Boulder, Colorado, USA, [3]Department of Geological Sciences, University of Colorado Boulder, Boulder, Colorado, USA, [4]Institute of Arctic and Alpine Research, University of Colorado Boulder, Boulder, Colorado, USA

Abstract We develop a multiproxy, reduced-dimension methodology to blend magnesium-calcium (Mg/Ca) and alkenone (U^{k}_{37}) paleo sea surface temperature (SST) records from the eastern and western equatorial Pacific, to recreate snapshots of full field SSTs and zonal winds from 10 to 2 ka B.P. in 2000 year increments. Single-proxy reconstructions (Mg/Ca only versus $U^{K'}_{37}$ only) reveal differences in the timing and duration of maximum cooling across the east-central equatorial Pacific. The largest zonal temperature differences (average west Pacific SST minus average east Pacific SST) occur at 6 ka B.P. for the Mg/Ca-only reconstruction (0.61°C) and at 10 and 4 ka for the $U^{K'}_{37}$-only reconstruction (0.55°C and 0.47°C, respectively). Disagreements between SST trends suggested by each proxy call for methods that can resolve the common patterns between each and have motivated the work presented in this study. In combining inferences from these proxies, we treat both Mg/Ca and $U^{K'}_{37}$ reconstructions of SST as annual average values, but we recognize that they may be sensitive to different seasons. In the multiproxy reconstruction, the zonal SST difference is largest at 10 ka (0.26°C), with coldest SST anomalies of ~ −0.9°C in the eastern equatorial Pacific and concurrent easterly maximum zonal wind anomalies of 7 m s^{-1} throughout the central Pacific. From 10 to 2 ka, the entire equatorial Pacific warms, but at a faster rate in the east than the west, and the average central Pacific easterly winds weaken gradually to approximately 2 m s^{-1}. These patterns are broadly consistent with previous inferences of reduced El Niño-Southern Oscillation variability associated with a "La Niña-like" state during the early to middle Holocene.

1. Introduction

Both numerical model simulations and paleoclimatic and paleoceanographic observations suggest that the equatorial Pacific is sensitive to changes in orbital insolation forcing across the Holocene. *Clement et al.* [1999, 2000] used the Zebiak-Cane model [*Zebiak and Cane*, 1987] to simulate both decreased El Niño–Southern Oscillation (ENSO) activity and a lower sea surface temperature (SST) in the eastern tropical Pacific during the early to middle Holocene. They attributed decreased ENSO activity to the lower SST, which they found to be due to greater heating during boreal summer and less during boreal winter. Most General Circulation Models (GCMs) also display reduced ENSO variance during the mid-Holocene (~6000 years ago, ka), likely due to stronger easterly winds that result from a stronger zonal SST gradient and should suppress the growth of El Niño events [*Otto-Bliesner et al.*, 2003; *Zheng et al.*, 2008], with the wind strengthening being at least partially linked to a stronger Asian summer monsoon [*Liu et al.*, 2000]. The mean state of equatorial Pacific sea surface temperatures (SSTs) during the early to middle Holocene was likely important for the ENSO system because of Bjerknes feedback whereby easterly wind strength is coupled to the SST field [*Bjerknes*, 1969], but the models provide no consensus on the zonal SST gradient during the early to middle Holocene.

Early paleoclimatic proxy-based efforts to reconstruct the ENSO system during the Holocene focused on archives that could record the signatures of individual events. Clastic sediment records from lakes in the Andes suggest increasing frequency of El Niño events since the mid-Holocene [*Moy et al.*, 2002; *Rodbell et al.*, 1999]. A single multidecadal coral snapshot of oxygen isotopes ($\delta^{18}O$) from ~6.5 ka reveals reduced ENSO activity [*Tudhope et al.*, 2001], as does a longer coral record from 4.3 ka [*McGregor et al.*, 2013] and coastal Peru mollusk $\delta^{18}O$ from 4.7 ka [*Carré et al.*, 2014], but the current state-of-the-art coral compilation reveals no apparent

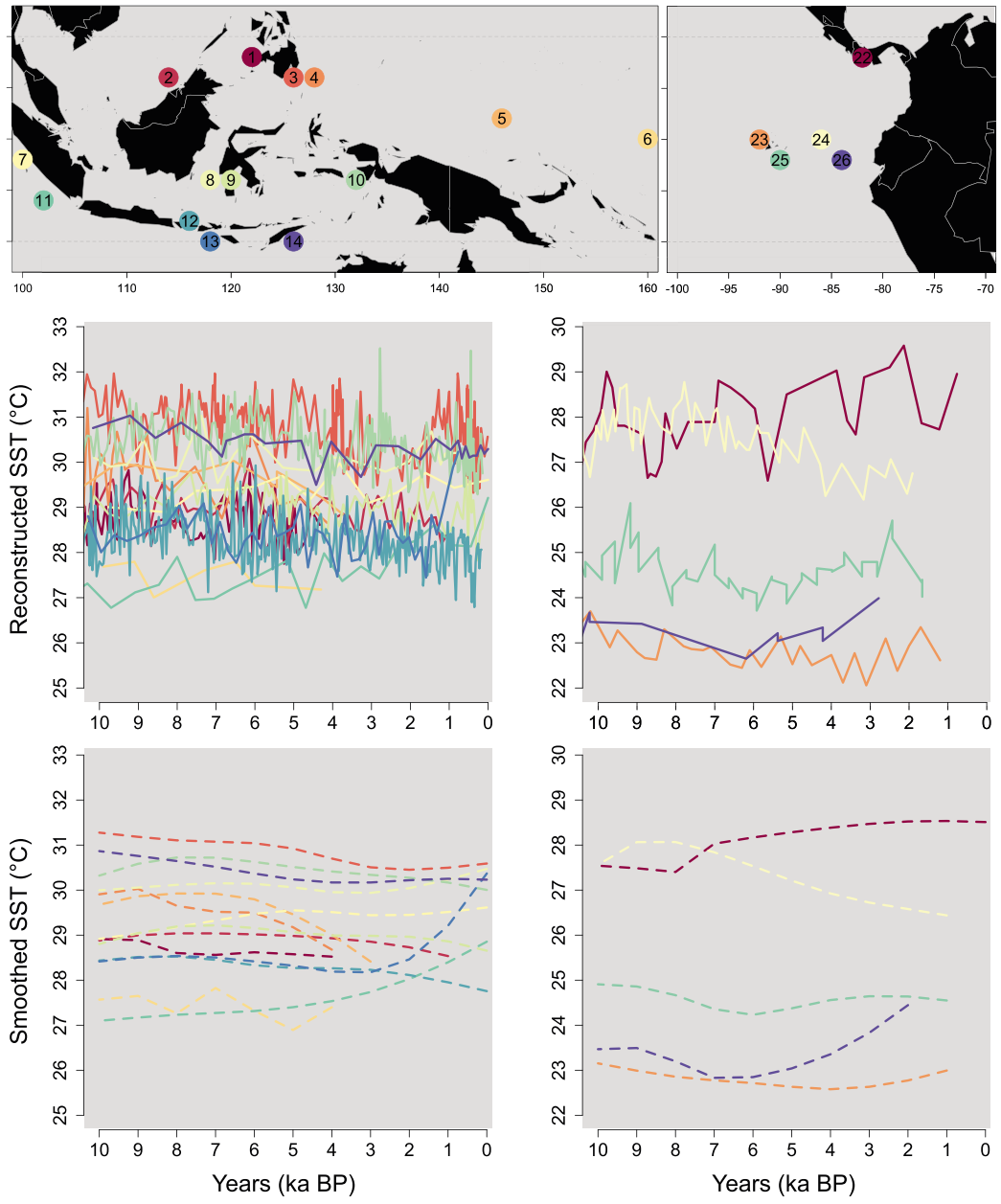

Figure 1. (top row) Maps of western and eastern Pacific Mg/Ca SST records. (middle row) Raw SST time series with updated calibrations. (bottom row) The records smoothed by a second order local polynomial method with a local neighborhood of 70% nearest data points.

orbital-scale trend in variability [*Cobb et al.*, 2013]. δ^{18}O measurements on individual planktonic foraminifera from the eastern equatorial Pacific cold tongue show decreased variance during the mid-Holocene, a pattern attributed to suppressed ENSO activity [*Koutavas et al.*, 2006; *Koutavas and Joanides*, 2012], but a change in seasonality could also contribute [*Thirumalai et al.*, 2013].

For the mean state of SSTs, the most useful proxies are planktonic foraminiferal Mg/Ca and alkenone unsaturation extracted from marine sediment cores. *Koutavas et al.* [2002] compared a single Mg/Ca record from the eastern cold tongue to a single alkenone record from the western warm pool and argued that the zonal SST gradient was larger during the mid-Holocene, a pattern that they dubbed "La Niña-like." Subsequent compilations based on Mg/Ca support this view [*Koutavas and Joanides*, 2012; *Marchitto et al.*, 2010], but some Mg/Ca records from the cold tongue do not support cooler temperatures during early Holocene as compared to present day (Figure 1). Additionally, Mg/Ca and alkenone records do not always agree with one another

Table 1. Western Equatorial (10°N–10°S) Pacific Proxy Records

Number	Core	Latitude	Longitude	Depth (m)	Original Calibration	Reference
			Mg/Ca Records, (Figure 1, Left Panel)			
1[a]	MD97 - 2141	8.80	121.30	3633	*Rosenthal and Lohmann* [2002]	*Rosenthal et al.* [2003]
2	MD01 - 2390	6.64	113.41	1545	*Dekens et al.* [2002]	*Steinke et al.* [2008]
3	MD98 - 2181	6.30	125.83	2114	*Nürnberg et al.* [1996]	*Stott et al.* [2004]
4[a]	MD06 - 3067	6.51	126.50	1575	*Anand et al.* [2003]	*Bolliet et al.* [2011]
5[a]	MD97 - 2138	1.25	146.14	1960	*de Garidel-Thoron et al.* [2005]	*de Garidel-Thoron et al.* [2007]
6[a]	ODP - 806b	0.32	159.35	2520	*Lea and Martin* [1996]	*Lea et al.* [2000]
7	GeoB 10029-4	−1.50	100.10	964	*Anand et al.* [2003]	*Mohtadi et al.* [2010]
8	MD98 - 2162	−4.69	117.90	1855	*Hastings et al.* [2001]	*Visser et al.* [2003]
9	70 GGC	−3.56	119.40	482	*Anand et al.* [2003]	*Linsley et al.* [2010]
10	MD98 - 2176	−5.00	133.45	2382	*Nürnberg et al.* [1996]	*Stott et al.* [2004]
11	GeoB 10038-4	−5.90	103.30	1819	*Anand et al.* [2003]	*Mohtadi et al.* [2010]
12	13 GGC	−7.40	115.20	594	*Anand et al.* [2003]	*Linsley et al.* [2010]
13	MD98 - 2165	−9.65	118.34	2100	*Dekens et al.* [2002]	*Levi et al.* [2007]
14	MD98 - 2170	−10.59	125.39	832	*Nürnberg et al.* [1996]	*Stott et al.* [2004]
			$U^{k'}_{37}$ *Records, (Figure 2, Left Panel)*			
15	GIK 18252-3	9.23	109.38	1273	*Pelejero and Grimalt* [1997]	*Kienast et al.* [2001]
16	MD97 - 2151	8.72	109.87	1598	*Pelejero and Grimalt* [1997]	*Zhao et al.* [2006]
17[a]	GIK 18287-3	5.65	110.65	598	*Pelejero and Grimalt* [1997]	*Kienast et al.* [2001]
18	GIK 17964	6.16	112.21	1556	*Müller et al.* [1998]	*Pelejero et al.* [1999]
19[χ^{-3}b]	MD06 - 3075	6.48	125.83	1878	*Sonzogni et al.* [1997]	*Fraser et al.* [2014]
20[a]	MD97 - 2138	1.25	146.14	1960	*Prahl et al.* [1988]	*de Garidel-Thoron et al.* [2007]
21	SO139 - 74KL	−6.54	103.83	1690	*Conte et al.* [2006]	*Lückge et al.* [2009]

[a]Records removed from single-proxy and multiproxy reconstructions because it did not extend to 2 ka B.P.
[b] $\chi^{-\#}$ denotes records that snap to the same grid cell as another record from the other proxy type (#) and are removed from the multiproxy reconstruction because they have the lower sample resolution of the two.

[e.g., *Leduc et al.*, 2010]. Given these conflicting indicators, we suggest that spatial reconstructions of mean equatorial Pacific SST fields would be beneficial, which motivates this work.

Paleoclimatic proxy data are intrinsically point measurements, and therefore associating one paleoclimate time series with a process that reaches over a huge area takes a risk. Moreover, because of dissolution of carbonate tests and low sedimentation rates at great water depths, useful cores for SST proxy records (Tables 1 and 2 and Figures 1 and 2) are typically limited to regions of relatively shallow depth, and therefore near coasts, from aseismic ridges or over young oceanic crust. As a result, the absence of long-term records from the central Pacific makes it difficult to draw conclusions about large-scale spatial patterns of SSTs over paleoclimatic timescales. The records that exist along the ocean margins are often irregularly sampled (spatially and temporally), and different proxies from the same core can sometimes yield contradictory inferences. Previous studies have used paleoproxy data with various statistical approaches to reconstruct full fields [e.g., *Cook et al.*, 1999; *Kaplan et al.*, 1998; *Luterbacher et al.*, 2004; *Mann et al.*, 1998, 2008; *Tingley and Huybers*, 2010] or time series [e.g., *Kaufman et al.*, 2009; *Lee et al.*, 2008; *Li et al.*, 2010; *Mann et al.*, 2008; *Moberg et al.*, 2005] of climate variables. Reduced-dimension approaches, in which contemporary patterns of variability are related to a sparse sampling of points to resolve full fields or time series of climate variables, have been used to reconstruct surface temperature [e.g., *Luterbacher et al.*, 2004; *Mann et al.*, 1998; *Rutherford et al.*, 2005], pressure [e.g., *Luterbacher et al.*, 2002], and drought [e.g., *Cook et al.*, 1999; *Zhang et al.*, 2004]. *Evans et al.* [2002] provide an example of a reduced-dimension SST field reconstruction using δ^{18}O proxy records from coral.

We develop and present the results of a reduced-dimension reconstruction approach based on principal component and canonical correlation analyses, to reconstruct equatorial Pacific mean SSTs and zonal winds over the Holocene. The method was applied to all available equatorial Pacific SST records from two common paleothermometric proxies: planktonic foraminiferal Mg/Ca and alkenone unsaturation.

Table 2. Eastern Equatorial (10°N–10°S) Pacific Proxy Records

Number	Core	Latitude	Longitude	Depth (m)	Original Calibration	Reference
			Mg/Ca Records, (Figure 1, Right Panel)			
22	ODP - 1242	7.86	−83.61	1364	*Anand et al.* [2003]	*Benway et al.* [2006]
23	TR163 - 22	0.52	−92.40	2830	*Dekens et al.* [2002]	*Lea et al.* [2006]
24	ODP - 1240	0.02	−86.45	2921	*Dekens et al.* [2002]	*Pena et al.* [2008]
25	V21 - 30	−1.22	−89.68	617	*Dekens et al.* [2002]	*Koutavas et al.* [2006]
26$^{\chi-35b}$	V19 - 28	−2.51	−84.65	2720	*Dekens et al.* [2002]	*Koutavas et al.* [2006]
			$U^{k'}_{37}$*Records, (Figure 2, Right Panel)*			
27	MD02 - 2529	8.21	−84.12	1619	*Sonzogni et al.* [1997]	*Leduc et al.* [2007]
28$^{\chi-22b}$	ME0005A - 43JC	7.85	−83.60	1368	*Prahl et al.* [1988]	*Dubois et al.* [2009]
29	KNR176 - JPC32	4.85	−77.96	2200	*Prahl et al.* [1988]	*Pahnke et al.* [2007]
30	TR163 - 19	2.25	−90.95	2348	*Prahl et al.* [1988]	*Dubois et al.* [2009]
31	ME0005A - 24JC	1.50	−89.68	2941	*Prahl et al.* [1988]	*Kienast et al.* [2006]
32$^{\chi-23b}$	TR163 - 22	0.52	−92.40	2830	*Prahl et al.* [1988]	*Dubois et al.* [2009]
33	V19 - 27	−0.47	−82.67	1373	*Prahl et al.* [1988]	*Koutavas and Sachs* [2008]
34$^{\chi-25b}$	V21 - 30	−1.22	−89.68	617	*Prahl et al.* [1988]	*Koutavas and Sachs* [2008]
35[a]	RC11 - 238	−1.52	−85.82	2573	*Prahl et al.* [1988]	*Koutavas and Sachs* [2008]
36	V19 - 28	−2.51	−84.65	2720	*Prahl et al.* [1988]	*Koutavas and Sachs* [2008]
37	ME0005A - 27JC	−1.85	−82.78	2203	*Prahl et al.* [1988]	*Dubois et al.* [2009]
38	V19 - 30	−3.38	−83.52	3091	*Prahl et al.* [1988]	*Koutavas and Sachs* [2008]
39	CDH - 26	−3.59	−81.18	1023	*Prahl et al.* [1988]	*Bova et al.* [2015]

[a]Records removed from single-proxy and multiproxy reconstructions because it did not extend to 2 ka B.P.
[b]$\chi^{-\#}$ denotes records that snap to the same grid cell as another record from the other proxy type (#) and are removed from the multiproxy reconstruction because they have the lower sample resolution of the two.

2. Data

2.1. Contemporary Data

The spatial domain for the reconstructions is 10°S to 10°N and 100°E to 75°W. We use gridded (2° by 2°) monthly SSTs from 1854 to 2013 from the NOAA National Climatic Data Center (NCDC) Extended Reconstruction Sea Surface Temperature (ERSST) version 3b data set [*Smith et al.*, 2008] and gridded (2.5° by 2.5°) monthly zonal winds from 1949 to 2013 from NOAA National Centers for Environmental Prediction (NCEP)-National Center for Atmospheric Research (NCAR) CDAS-1 Global Reanalysis [*Kalnay et al.*, 1996]. We calculate monthly anomalies for each data set using a 1981–2010 climatology. By averaging from May to the following April, we convert monthly anomalies of SSTs and winds into annual averages that capture the annual ENSO cycle.

2.2. Collection and Treatment of Paleo SST Data

One common proxy for paleothermometry exploits Mg/Ca ratios from planktonic foraminifera shells, such as *Globigerinoides ruber*, extracted from deep-sea sediment cores. At high temperatures, more Mg is incorporated in the shells of foraminifera, and a ratio of Mg/Ca can be used to infer SSTs back through time [e.g., *Lea et al.*, 1999; *Nürnberg et al.*, 1996]. Paleo SST records can also be inferred using alkenones produced by some species of coccolithophores (unicellular eukaryotic phytoplankton), such as *Emiliana huxleyi*. Alkenones are transfat altered under various temperatures: lower temperatures lead to an increase in the degree of unsaturation. The ratio of ditriunsaturated ($C_{37:2}$) to triunsaturated ($C_{37:3}$) alkenones is used to create an Alkenone Unsaturation Index named $U^{k'}_{37}$ (= $C_{37:2}/(C_{37:2} + C_{37:3})$) [e.g., *Brassell et al.*, 1986; *Herbert*, 2003], which scales directly to SSTs. Numerous Mg/Ca and $U^{k'}_{37}$ proxy records have been reported for the east and west Pacific [see *Leduc et al.*, 2010, for a review]. Mg/Ca (Figure 1) and alkenone (Figure 2) SST records for the west (Table 1) and east (Table 2) equatorial Pacific were obtained from the archives of NCDC (http://www.ncdc.noaa.gov/data-access/paleoclimatology-data/datasets) and Pangaea (http://www.pangaea.de/). Although coral archives enable reconstructions of ENSO variability, they are less useful for assessing millennial-to-orbital-scale means because of the brief windows of time that they capture (leading to potential aliasing of multidecadal-scale variability [cf. *Mann et al.*, 2005]), and because of their apparent inability to capture centennial-scale and longer trends [e.g., *Emile-Geay et al.*, 2013].

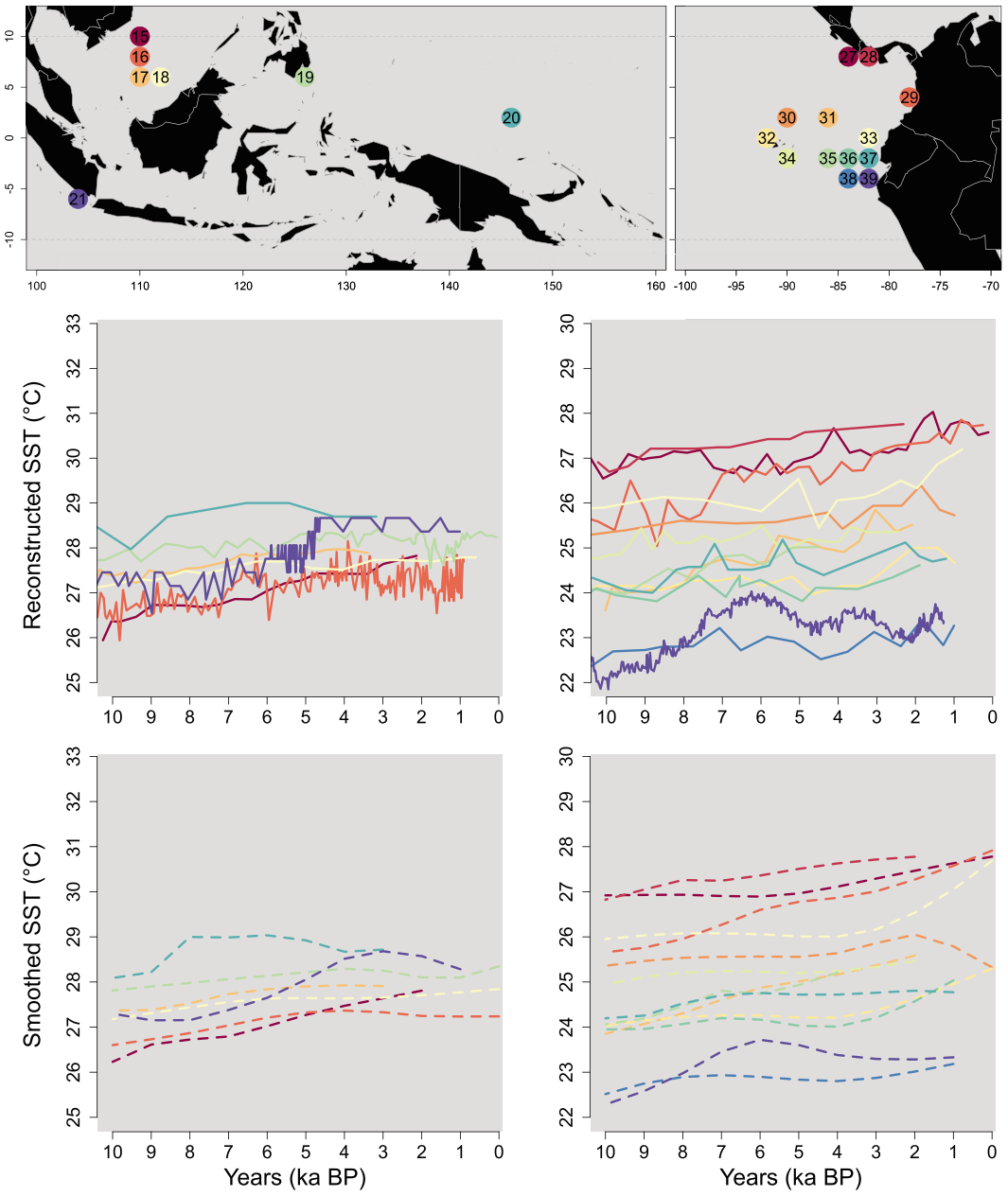

Figure 2. Maps of western and eastern Pacific $U^{k'}_{37}$ SST records. Layout is the same as in Figure 1.

Records reported in Tables 1 and 2 were originally published using a variety of calibration equations for both proxies. For intraproxy comparison, we recalibrated all of the records using a single alkenone and a single Mg/Ca calibration. For alkenones, most use the global mean annual SST equation first found through experimental analysis [*Prahl et al.*, 1988] and later corroborated by core-top calibrations [*Müller et al.*, 1998] and sediment trap data [*Rosell-Melé and Prahl*, 2013]. We recalibrated all alkenone records using the authors' reported $U^{k'}_{37}$ data with the calibration of *Müller et al.* [1998]: ($U^{k'}_{37} = 0.033\ SST(°C) + 0.044$).

There is less consensus within the Mg/Ca community on a single-calibration equation, mainly due to the obstacle of accounting for dissolution effects, which depend in part on the location and depth of the sediment core. Dissolution of calcite occurs when the in situ concentration of carbonate ion is less than the saturation concentration of carbonate ion ($\Delta CO_3^{2-} = [CO_3^{2-}]_{insitu} - [CO_3^{2-}]_{saturation}$) [*Berger et al.*, 1982]. Since dissolution is typically greater in the deep ocean due to the increase of $[CO_3^{2-}]_{saturation}$ with pressure, there exist calibration equations that use depth of core retrieval as a proxy for dissolution. However, such equations do not

adequately control for spatial variations in $[CO_3^{2-}]_{insitu}$, which tends to decrease as deep waters accumulate respired CO_2. Therefore, we used the calibration equation of *Dekens et al.* [2002], which directly incorporates a correction for ΔCO_3^{2-}: $Mg/Ca = 0.33 \exp [0.09 [SST(°C) + 0.042(\Delta CO_3^{2-})]]$. By using modern estimated bottom water ΔCO_3^{2-} for these corrections, we implicitly assume that temporal variations in saturation have been minimal within the Holocene and that sediment pore waters are not appreciably decoupled from bottom waters. Corrections could presumably be improved by using dissolution proxy records [e.g., *Mekik et al.*, 2007], but such data are available from only one of the cores compiled here (#23) where it was argued to have no significant impact on Mg/Ca [*Lea et al.*, 2006].

For each Mg/Ca core site, we collected total dissolved inorganic carbon and alkalinity data from GLODAP (www.cdiac.ornl.gov/oceans/glodap/data_files.html) and modern day ocean temperature, salinity, pressure, dissolved phosphate, and dissolved silicate from the World Ocean Database (www.nodc.noaa.gov/OC5/WOD13/). For a few of the western Pacific locations for which there are no nearby GLODAP data (MD98-2162, 70GGC, 13GGC, MD98-2176), we used throughflow current maps to estimate total carbon and alkalinity. These data were used along with the program CO2SYS v.2.1 [*Lewis and Wallace*, 1998] using the default values for dissociation constants [*Mehrbach*, 1973, as refit by *Dickson and Millero*, 1987] to calculate estimates of ΔCO_3^{2-} for each core site.

We treat all inferences of SSTs from both alkenone $U_{37}^{k'}$ measurements and Mg/Ca ratios as annual averages. We are aware that doing so carries some risk, because each might be sampling a different season, for a number of studies have pointed out disagreements in inferred SSTs from the two proxies [e.g., *Haug et al.*, 2005; *Leduc et al.*, 2010; *Timmermann et al.*, 2014]. Although $U_{37}^{k'}$ indices core top sediment match annual average SSTs in some regions [e.g., *Chen et al.*, 2007; *Dekens et al.*, 2002; *Müller et al.*, 1998; *Rosell-Melé and Prahl*, 2013; *Sonzogni et al.*, 1997], in some they fit better with warm seasons [e.g., *Harada et al.*, 2001; *Haug et al.*, 2005; *Leduc et al.*, 2010; *Schneider et al.*, 2010; *Steinke et al.*, 2008; *Timmermann et al.*, 2014; *Wang et al.*, 2013], if elsewhere, they do with colder seasons [e.g., *Chen et al.*, 2007]. Moreover, there seem to be depth differences sampled by the coccolithophores in which the alkenones formed [*Ohkouchi et al.*, 1999]. All of this can be rendered yet more complicated, because other plankton, like diatoms, can bloom in the same season that is ideal for coccolithophores but consume most of the nutrients [e.g., *Harada et al.*, 2001; *Schneider et al.*, 2010]. Similarly, for some regions, the foraminifera on which Mg/Ca measurements are made also bloom primarily in one season, and they too suggest a preference for that season [e.g., *Ashkenazy and Tziperman*, 2006; *Nürnberg et al.*, 2000; *Thunell and Reynolds*, 1984; *Wang et al.*, 2013]. Attempts to exploit seasonal sampling of SSTs by alkenones and Mg/Ca measurements have led to some success. For instance, *Timmermann et al.* [2014] found that their model calculations for the warm season in the eastern tropical Pacific matched $U_{37}^{k'}$ measurements from alkenones well, but for the western Pacific, the match for both alkenones and Mg/Ca was less impressive. Because of the inconsistent results, we refrain from assuming that alkenones and Mg/Ca measurements sample specific seasons.

We include records only from our equatorial Pacific domain (10°S to 10°N and 100°E to 75°W) and with temporal resolutions of at least one value per 1000 years. We smoothed all records (Figures 1 and 2) using a local polynomial method with a second-order polynomial and a local neighborhood consisting of 70% of the nearest data points [e.g., *Loader et al.*, 1996] in order to obtain a value for each record representative of 2, 4, 6, 8, and 10 ka. Note that smoothed records that stop prior to 2 ka are plotted but were removed from the spatial field reconstructions (denoted by an alpha symbol on Tables 1 and 2). All records that included data equal to or younger than 2 ka B.P. were smoothed to 0 ka. Records were then converted to SST anomalies using the 0 ka temperature from each smoothed proxy record.

3. Methods for Reconstruction

Our work is rooted in similar methodologies and assumptions made by *Mann et al.* [1998], who used a multiproxy, reduced-dimension approach to combine instrumental records with proxies from tree rings, ice cores, and corals to reconstruct global annual temperature patterns over the past six centuries. We used a principal component analysis (PCA) approach (Figure 3) to reconstruct SSTs and a canonical correlation analysis (CCA) approach to reconstruct zonal wind speeds.

3.1. Principal Component Analysis (PCA) and Canonical Correlation Analysis (CCA)

In PCA, multivariate space-time data are decomposed into orthogonal space-time components via eigen decomposition of the covariance matrix. These components, also referred to as patterns or modes, are ordered

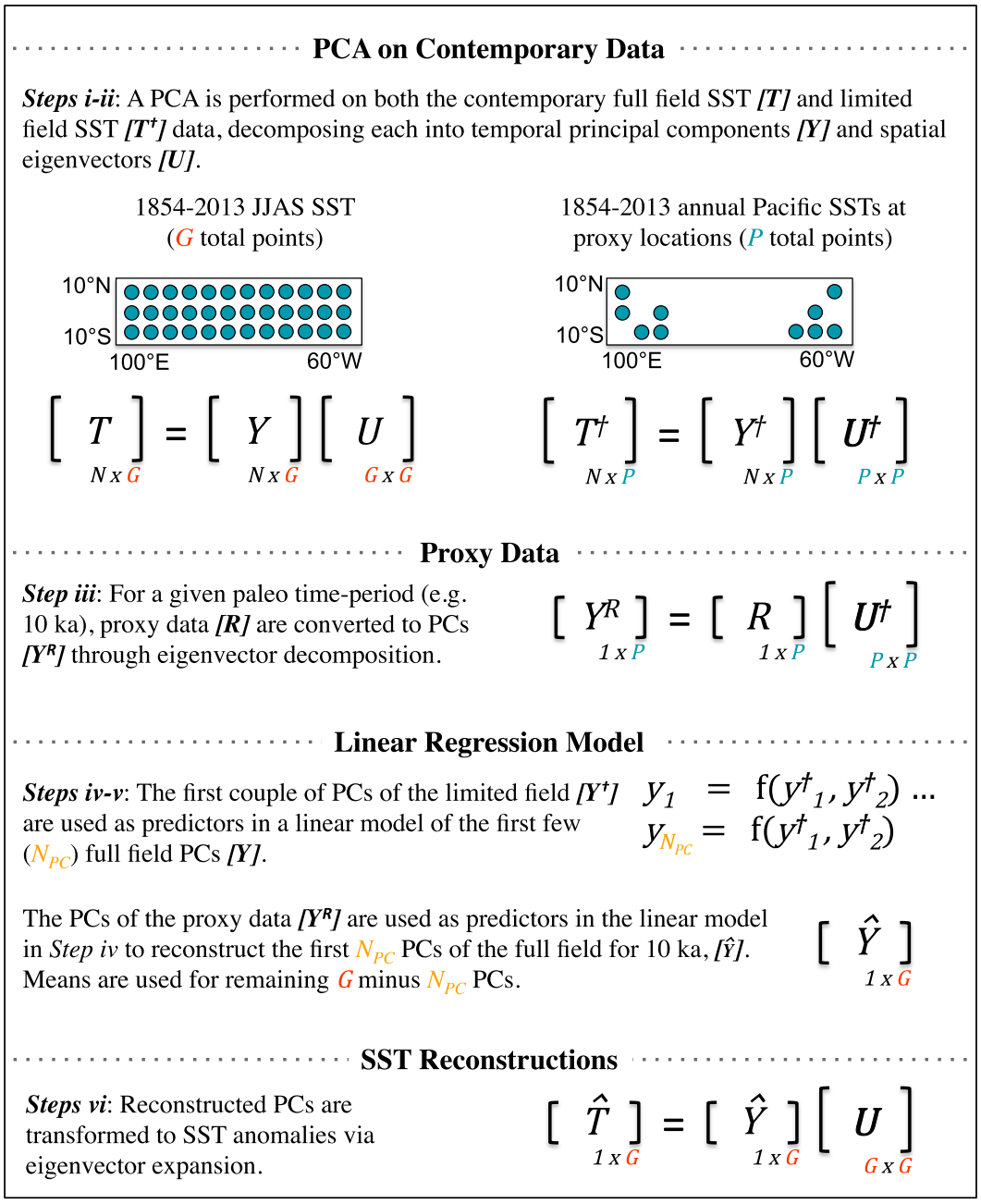

Figure 3. Diagram of methodology used in PCA-based reconstruction.

based on the percentage of total variance that each resolves. For most climatological data sets, the first few modes capture the majority of the data variance—thus reducing the dimension of the data. Using bold-faced uppercase variables to denote matrices, with brackets used only when specifying the dimensions of the matrix, and lowercase bold-faced variables as vectors, the formulation for a PCA is as follows:

$$[\boldsymbol{X}]_{N\times G} = [\boldsymbol{Y}]_{N\times G}[\boldsymbol{U}]_{G\times G} \quad (1)$$

$$[\boldsymbol{Y}]_{N\times G} = [\boldsymbol{X}]_{N\times G}[\boldsymbol{U}]^{T}_{G\times G} \quad (2)$$

where $\boldsymbol{X}$ is the matrix of the original data (e.g., SST), $\boldsymbol{Y}$ is a matrix of principal components (PCs), $\boldsymbol{U}$ is a matrix of eigenvectors, N is the length of data at each location (i.e., number of times sampled), and G is the number of grid points. $\boldsymbol{U}$ is considered a transformation matrix, as it transforms the correlated data $\boldsymbol{X}$ into orthogonal

principal component (PC) space of $\boldsymbol{Y}$ or transforms the PCs back into the data space. In theory, the eigenvectors are obtained sequentially by solving a constrained optimization problem. The first eigenvector, $\boldsymbol{u}_1$, is found by minimizing the mean squared error $\epsilon_1 = E[\boldsymbol{X} - \boldsymbol{X}\boldsymbol{u}_1]^2$ subjected to the orthonormality constraint of $\boldsymbol{u}_1\boldsymbol{u}_1^T = 1$. The subsequent eigenvectors are obtained to minimize successively the residual mean squared errors. Thus, the variance of all the PCs sums to the variance of the original data. *Von Storch and Zwiers* [2001] give details of PCA and other multivariate analysis techniques. In practice, eigenvectors are obtained simultaneously by an eigen decomposition of the covariance matrix of $\boldsymbol{X}$. The steps of this method as applied to our reconstruction are described briefly below, and further details are given in Appendix A along with a schematic in Figure 3.

For the SST reconstruction, a PCA is performed on the full field of equatorial Pacific instrumentally measured SSTs. The first three modes are retained, which jointly explain 87% of the present-day variability (Figure A1). A PCA is then performed on the "limited field," a field of present-day SSTs only at the locations for which either an Mg/Ca or $U_{37}^{K'}$ proxy record exists (Figure A1). We retain the first two modes of the limited field PCA: jointly they explain 92% of the variance. Using linear regression, we relate each of the three PCs of the full field to the two PCs of the limited field. For a given paleo time, say 10 ka, we multiply paleo SST anomalies (one value at each point in the limited field) by the contemporary limited field eigenvector matrix. Multiplying by this transformation matrix converts the limited field paleo SSTs to limited field paleo PCs. The first two limited field paleo PC values in conjunction with the linear regression models provide estimates of the first three full-field paleo PC values for 10 ka. Recall, however, that G total PCs are needed to reconstruct the full field. For the remaining full-field paleo PCs, we use average values from the full-field contemporary PCs, each of which essentially equals zero. This procedure is repeated for 8, 6, 4, and 2 ka.

For the wind field reconstruction, the CCA method is quite similar to the PCA-based method depicted in Figure 3 and described above. CCA, however, is preferred over standard PCA in a scenario such as this where the patterns of one variable, e.g., SSTs, are used as predictors of patterns of a related variable, e.g., zonal winds. This method is widely used for multisite forecasting of precipitation [e.g., *Barnston*, 1994; *Barnston and Smith*, 1996], temperature [e.g., *Barnett and Preisendorfer*, 1987; *Barnston*, 1994; *Barnston and Smith*, 1996; *Mo*, 2003], streamflow [e.g., *Salas et al.*, 2010], and SSTs [e.g., *Barnston and Ropelewski*, 1992]. See Appendix A as well as *Bretherton et al.* [1992], *Von Storch and Zwiers* [2001], and *Cherry* [1996] for details on CCA. Here we use SST patterns to reconstruct zonal winds across the equatorial Pacific. We choose to reconstruct zonal winds in this region as they are much larger than meridional winds.

3.2. Calibration of PCA and CCA Models

In Appendix A, we describe calibration and validation tests performed to assess the reliability of the procedure to reproduce contemporary SSTs and zonal winds. Here we show results of a comparison between the actual and reconstructed SST and zonal wind fields for the anomalous ENSO years of 1988–1989 (strong La Niña with standardized SST anomalies of −1.5°C in the NINO3 index region of 150°W–90°W and 5°S–5°N) and 1997–1998 (strong El Niño with standardized NINO3 index SST anomalies of +2.8°C). For 1988–1989, the procedure captures anomalies slightly cooler than −1°C, which are not as cold and do not extend as far westward as the actual anomalies seen during this particular La Niña year (Figure 4, top). The reconstructed zonal wind pattern for this year defines a shape similar to that of actual zonal winds, with negative anomalies (strengthened easterlies) across the central Pacific and into the western Pacific north of the equator, and with positive anomalies over the Indonesian archipelago (Figure 4, top). The reconstruction captures the regions of −2.5 m s^{-1} anomalies in the western Pacific north of the equator but misses the zone of strongest easterlies (3.5 m s^{-1}) in the central Pacific. The negative anomalies in winds over the far eastern Pacific off the coast of South America are not captured by the reconstruction, which is consistent with the relatively low statistical measures of fit, β and R^2 values, seen in that region (Figure A4).

The reconstructed magnitudes and spatial patterns of anomalous SSTs match those of the strong El Niño year of 1997–1998 (Figure 4, bottom), better than those for 1988–1989. Consistent with the observed warming, the reconstructed anomalous warming extends just west of the dateline; the greatest magnitude of warming, which is off the coast of Peru in the far eastern Pacific, reaches approximately +3.5°C; and the distribution of temperatures within the reconstructed "warm tongue" closely resemble those of the observed SSTs. It is likely that the failure of the limited-field model to capture La Niña SST anomalies across the entire Pacific is due to the restricted locations of the proxy records. The cold La Niña anomaly of 1988–1989 is centered in the east-central Pacific, where there are no proxy records. The maximum warm anomaly of the 1997–1998

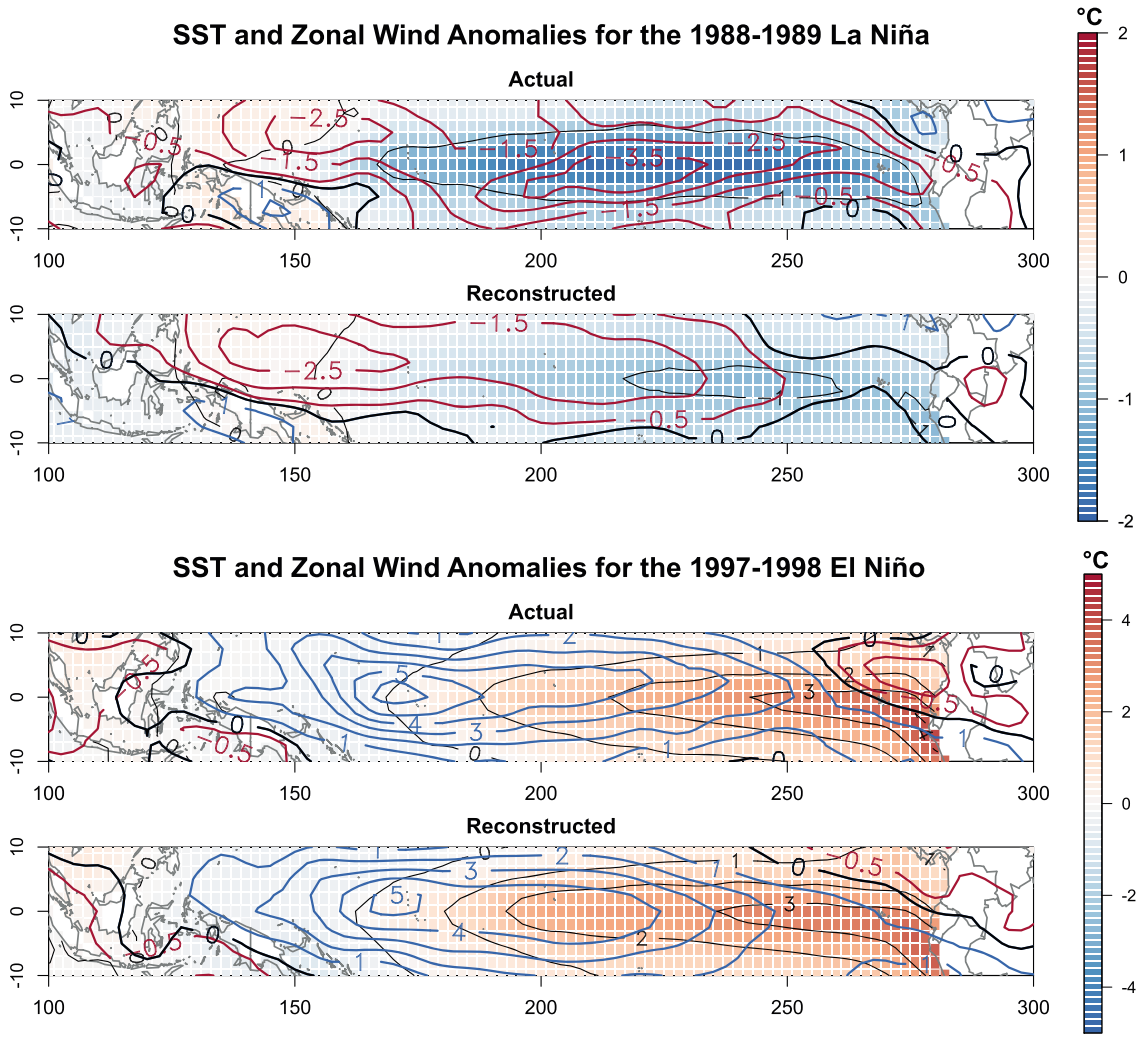

Figure 4. Actual and reconstructed SST anomalies (°C; shading and thin black contouring) and zonal wind anomalies (m s^{-1}; red and blue contouring) for (top) 1988–1989 (a strong La Niña year) and for (bottom) 1997–1998 (a strong El Niño year). Easterlies (westerlies) are shown by negative (positive) zonal wind anomalies and red (blue) contouring.

El Niño anomaly, however, is located in the far eastern Pacific, which the paleoceanographic data sample well. Reconstructed winds for the El Niño year are arguably better than those for the La Niña year as well. The spatial patterns resemble one another, and the magnitude of maximum easterlies (5 m s^{-1}) is captured by the reconstruction (Figure 4, bottom).

3.3. Assumptions

Implicit in this approach are a few assumptions. First, we assume that spatial patterns of the proxy network are linearly related to spatial patterns of the full-field during the contemporary period. Second, we assume that the dominant space-time patterns of variability that exist in the contemporary data set are present over the past 10 ka. *Molnar and Cane* [2002, 2007] showed that ENSO teleconnection patterns of the present-day seem to have existed as far back as the early Pliocene (~5 Ma), suggesting that the dominant patterns of variability have not changed significantly over the relatively short period of time considered in this analysis. Third, we do not attempt, or claim, to reconstruct ENSO variability as the sampling resolution of deep-sea sediment cores is too low to capture the timescales required to assess long-term changes in ENSO variability. A La Niña-like mean cooling pattern could hypothetically be achieved by stronger and/or more frequent La Niña events, weaker and/or less frequent El Niño events, or simply an average cooling with no change in interannual variance. We do not distinguish between these possibilities in reconstructing mean states.

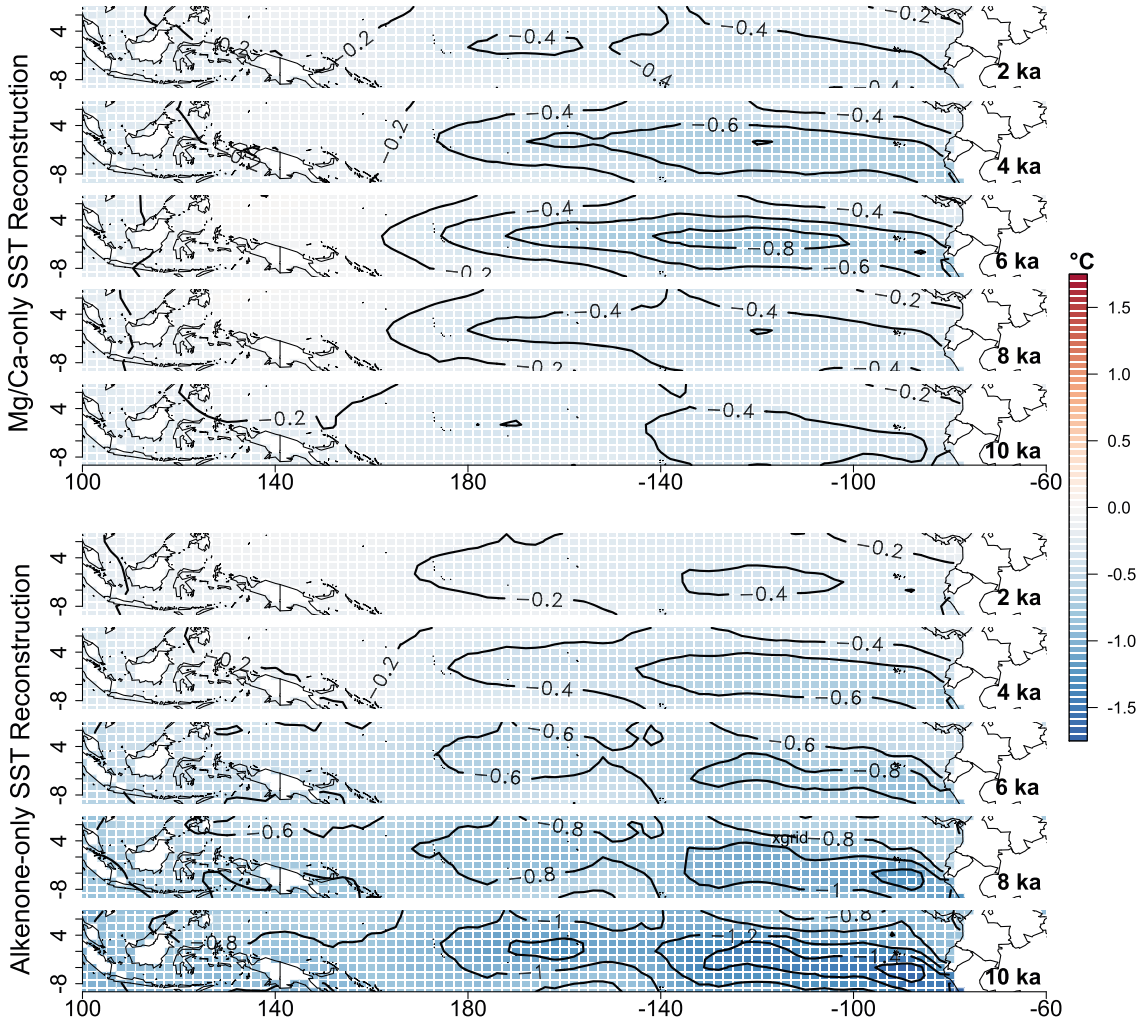

Figure 5. Single proxy reconstructions of 10, 8, 6, 4, and 2 ka equatorial Pacific SST anomalies using only (top) Mg/Ca proxies and (bottom) $U^{k'}_{37}$.

4. Results

4.1. Single Proxy Reconstructions of SSTs

It is clear from Figures 1 and 2 that for a given location, records based on different proxies are not always consistent. It follows that the spatial fields reconstructed by only Mg/Ca or $U^{k'}_{37}$ proxies should differ as well. To compare the two, we use 15 Mg/Ca records (10 in the western Pacific and 5 in the eastern Pacific) and 17 $U^{k'}_{37}$ records (5 in the western Pacific and 12 in the eastern Pacific) to obtain separate reconstructions of SST fields through the past 10 ka as implied by each proxy (Figure 5).

The zonal difference in SSTs from west to east is also of interest, as some [e.g., *Koutavas et al.*, 2002, 2006; *Koutavas and Joanides*, 2012] have argued that an "enhanced zonal gradient" characterized the early to middle Holocene equatorial Pacific. To quantify such gradients, Table 3 provides various indices throughout the Pacific: WPAC, NINO4, NINO3.4, NINO3, NINO1+2, TNI, and WTNI. The domain used in calculating each index is provided in the notes of Table 3. The TNI index quantifies the zonal SST difference by subtracting NINO1+2 from NINO4. The NINO4 region, however, contains no proxy records. For this reason, we also report a difference index called the WTNI, which is calculated by subtracting NINO1+2 from the WPAC (120°E to 180°E and 4°S to 4°N).

SST reconstructions based on either Mg/Ca or $U^{k'}_{37}$ show negative anomalies throughout 10–2 ka, with weak negative anomalies at 2 ka (~−0.2 to −0.4°C), consistent with warming since that time. They differ, however, in magnitude and in timing of the coldest anomalies. First, for Mg/Ca, the coldest eastern equatorial SST anomalies defined a marked "cold tongue" pattern at 6 ka, which is also the period of largest zonal difference

Table 3. Reconstructed SST Anomalies for Various NINO Indices

	Single Indices					Trans-Pacific Indices	
ka B.P.	WPAC	NINO4	NINO3.4	NINO3	NINO 1 + 2	TNI	WTNI
			Mg/Ca-Only Reconstruction				
10	−0.21 ± 0.12	−0.33 ± 0.18	−0.40 ± 0.17	−0.41 ± 0.17	−0.37 ± 0.26	0.04 ± 0.32	0.16 ± 0.29
8	−0.10 ± 0.13	−0.34 ± 0.18	−0.48 ± 0.17	−0.50 ± 0.17	−0.43 ± 0.27	0.09 ± 0.33	0.33 ± 0.30
6	−0.08 ± 0.13	−0.45 ± 0.18	−0.69 ± 0.17	−0.73 ± 0.17	−0.69 ± 0.26	0.24 ± 0.32	0.61 ± 0.29
4	−0.18 ± 0.13	−0.45 ± 0.18	−0.63 ± 0.17	−0.67 ± 0.17	−0.66 ± 0.27	0.21 ± 0.32	0.48 ± 0.29
2	−0.19 ± 0.13	−0.34 ± 0.19	−0.43 ± 0.18	−0.45 ± 0.17	−0.40 ± 0.27	0.06 ± 0.32	0.22 ± 0.29
			U^{k}_{37}-Only Reconstruction				
10	−0.85 ± 0.13	−1.05 ± 0.19	−1.21 ± 0.19	−1.28 ± 0.19	−1.40 ± 0.28	0.35 ± 0.34	0.55 ± 0.31
8	−0.71 ± 0.13	−0.84 ± 0.19	−0.92 ± 0.18	−0.97 ± 0.18	−1.04 ± 0.29	0.21 ± 0.34	0.33 ± 0.32
6	−0.51 ± 0.12	−0.61 ± 0.18	−0.68 ± 0.17	−0.73 ± 0.17	−0.76 ± 0.27	0.15 ± 0.32	0.26 ± 0.29
4	−0.19 ± 0.13	−0.41 ± 0.19	−0.57 ± 0.18	−0.63 ± 0.18	−0.67 ± 0.28	0.26 ± 0.34	0.47 ± 0.31
2	−0.12 ± 0.12	−0.24 ± 0.19	−0.33 ± 0.18	−0.36 ± 0.17	−0.35 ± 0.27	0.11 ± 0.33	0.23 ± 0.29
			Multiproxy Reconstruction				
10	−0.42 ± 0.13	−0.54 ± 0.19	−0.66 ± 0.18	−0.73 ± 0.18	−0.80 ± 0.27	0.26 ± 0.33	0.38 ± 0.30
8	−0.33 ± 0.12	−0.43 ± 0.18	−0.51 ± 0.17	−0.55 ± 0.17	−0.57 ± 0.27	0.14 ± 0.33	0.24 ± 0.30
6	−0.25 ± 0.13	−0.37 ± 0.18	−0.45 ± 0.17	−0.47 ± 0.17	−0.46 ± 0.26	0.08 ± 0.31	0.21 ± 0.29
4	−0.19 ± 0.12	−0.38 ± 0.18	−0.49 ± 0.18	−0.52 ± 0.17	−0.28 ± 0.27	0.01 ± 0.32	0.09 ± 0.29
2	−0.15 ± 0.12	−0.29 ± 0.18	−0.35 ± 0.18	−0.35 ± 0.17	−0.28 ± 0.26	0.01 ± 0.32	0.13 ± 0.29

in SSTs of 0.61°C ± 0.29°C (WTNI, Table 3). For $U^{k'}_{37}$, however, maximum eastern equatorial SST anomalies (−1.4°C ± 0.28°C in NINO1+2 region) and largest zonal differences (0.55°C ± 0.31°C WTNI) occur at 10 ka. There is an additional period of relatively large zonal differences shown by $U^{k'}_{37}$ at 4 ka (0.47°C ± 0.31°C). *Leduc et al.* [2010] noted that greater magnitudes of Holocene SST trends are observed in alkenone records than in Mg/Ca records, which is quantified by the reconstructions that were obtained.

In both proxies, the western Pacific is always warmer than the eastern Pacific. The evolution of western Pacific SSTs, however, differs between the two proxies. In the Mg/Ca reconstruction, the western Pacific is warmer at 6 ka than it is from 4–2 ka, which contributes to the larger zonal difference during this time. For $U^{k'}_{37}$ the west Pacific generally follows the eastern Pacific with a gradual warming trend from 10 to 2 ka, though with a smaller magnitude than in the east.

By compositing many of the same Mg/Ca and $U^{k'}_{37}$ SST time series from the east and west Pacific as are used in this study, *Timmermann et al.* [2014] found that although alkenones show continuous warming throughout the Holocene, Mg/Ca suggests net cooling from 8 ka to present. Our alkenone spatial reconstruction agrees with theirs, but our Mg/Ca differs in showing overall warming after 6 ka. This discrepancy may be attributed to the greater weight that our method gives to the five eastern Mg/Ca records, compared to the simple averaging of three cores by *Timmermann et al.* [2014].

As noted above, divergent behavior from these two proxies not only has been cited extensively but also has been commonly attributed to seasonal biases between the two, with alkenones commonly associated with warm seasons and, Mg/Ca, if perhaps less commonly, associated with cold seasons [e.g., *Chen et al.*, 2007; *Harada et al.*, 2001; *Haug et al.*, 2005; *Leduc et al.*, 2010; *Schneider et al.*, 2010; *Steinke et al.*, 2008; *Timmermann et al.*, 2014; *Wang et al.*, 2013]. Thus, it is possible that such seasonal biases influence the differing trends shown in Figure 5. As an example, if one assumes that alkenones preferentially sample boreal winter and Mg/Ca preferentially sample boreal summer across the tropical Pacific, then the single proxy reconstructions would suggest a stronger warming trend to present day from 10 ka during boreal winter than that of boreal summer. Since seasonality patterns between the two proxies for the east and west Pacific remain inconsistent, we refrain from drawing seasonal inferences from the single proxy reconstructions.

Divergent behavior from these two proxies is not surprising and has been cited extensively, particularly in terms of seasonal biases between the two [e.g., *Leduc et al.*, 2010; *Rosell-Melé and Prahl*, 2013;

Schneider et al., 2010; *Timmermann et al.*, 2014]. *Leduc et al.* [2010] attributed diverging patterns between $U^{k'}_{37}$ and Mg/Ca with the out-of-phase trends in seasonal insolation during the Holocene, noting that sometimes, but not always, alkenone records follow January insolation, while Mg/Ca records tend to follow June insolation. From a recent analysis of near-surface monthly chlorophyll concentration (as a proxy for primary productivity) and average monthly SSTs, *Timmermann et al.* [2014] inferred that alkenones (Mg/Ca) in the west (east) Pacific have a strong bias toward boreal winter (summer). For western Pacific Mg/Ca and eastern Pacific alkenones, the seasonal biases are less clear. In any case, it is possible that such seasonal biases influence the differing trends shown in Figure 5. Unfortunately, it is presently not possible to determine which of these reconstructions is the more representative of the true Holocene SST evolution.

4.2. Multiproxy Reconstructions of SSTs and Zonal Winds

Given the discrepancies between various proxy data, paleoceanographers are faced with a problem: How do we take advantage of all available data despite the differences between different proxies? One solution is to combine them using multiproxy reduced dimension methods. In fact, *Timmermann et al.* [2014] showed that combinations of alkenone and Mg/Ca can be used to gain insights into mean annual SST. By combining all records, we can extract features common to the two proxies. We emphasize that this method does not merely yield an average of the Mg/Ca and $U^{k'}_{37}$ reconstructions. Instead, eigenvectors weight each individual location's contribution to the overall spatial field. Therefore, proxy records are weighted based on location and not on proxy type. Accordingly, including all the proxy records together allows for wider coverage in both space and time. We do not know which reconstruction better represents the evolution of Holocene SSTs, but this approach provides a possible solution to dealing with multiple types of proxy data.

We reconstructed full-field SSTs and zonal winds for 10, 8, 6, 4, and 2 ka (Figure 6, top) using the multiproxy approach outlined above. The multiproxy SST reconstructions show the far eastern Pacific to have been a maximum of about 0.9°C cooler than today at 10 ka, along with a cold tongue anomaly, cooler by 0.7°C, extending to about 140°E. The western Pacific, however, also was cooler, by 0.4°C, for the same time period, resulting in a maximum zonal difference anomaly of 0.38 ± 0.30°C WTNI (Table 3). From 10 to 6 ka, the eastern Pacific warmed by about 0.4°C and the central and western Pacific warmed by about 0.2°C. By 2 ka, most of the domain was within −0.2 to −0.4°C of modern, with a zonal difference indistinguishable from today. Overall, the multiproxy patterns resemble more the $U^{k'}_{37}$ reconstruction than those from Mg/Ca, likely because of the greater number and consistency of alkenone records in the crucial eastern region.

The multiproxy reconstruction of winds (Figure 6, bottom) reveals maximum easterly wind anomalies (large negative zonal winds) at 10 ka, concurrent with the period of coolest SSTs in the eastern Pacific, and consistent with stronger easterlies seen during present-day La Niña events. Consistently throughout the reconstructions, the zone of strongest easterly wind anomalies is centered around 160°W. Easterlies are strongest at 10 ka, as much as 7 m s^{-1} stronger than present. Between 10 and 2 ka, the difference between past and present winds gradually decreases, and the location of the maximum difference moves slightly eastward.

A comparison of multiproxy reconstructed SST values with individual proxy SST anomalies from the eastern (Figure 7) and western (Figure 8) Pacific reveals better matches at some locations than others, which we quantify with the residual sum of squares (RSS) in the top right of each scatterplot. Recall that the first two modes of the limited field were used as predictors of SSTs. The values of the first and second eigenvectors at each particular location given under each scatterplot help explain why some proxy records are replicated better than others. These eigenvector (or EOF) values correspond to those plotted in Figure A1. Although not always the case, high RSS values, and hence poor fits, can often be attributed to low EOF values assigned to those locations, which implies that these data contributed little to the reconstructed SST fields. More commonly, the highest RSS values are calculated from records that are outliers from neighboring records, those that show greater anomalies over the past 10 ka than neighboring records do. For example, out of all eastern Pacific records (Figure 7), the worst fits (highest RSS values) are observed with proxies #24 (Mg/Ca, RSS = 26.85 °C^2), #33 ($U^{k'}_{37}$, RSS = 14.19 °C^2), and #29 ($U^{k'}_{37}$, RSS = 14.09 °C^2). The poor fit of #24 is not surprising, as it shows an overall trend opposite to the rest of the records in the eastern Pacific. Although records #33 and #29 show warming trends since 10 ka, which is consistent with the majority of the eastern Pacific records, SST anomalies at 10 ka are cooler than −1.5°C, which makes these records more negative than the others. Additionally, #29 has a relatively low EOF1 value for the eastern Pacific, which could contribute to a higher RSS value as well. It is worth noting that local processes occurring on a subgrid level (e.g., coastal processes) would not be captured by the PCA but could be recorded by proxy SST records. With this in mind, it is possible that the extreme

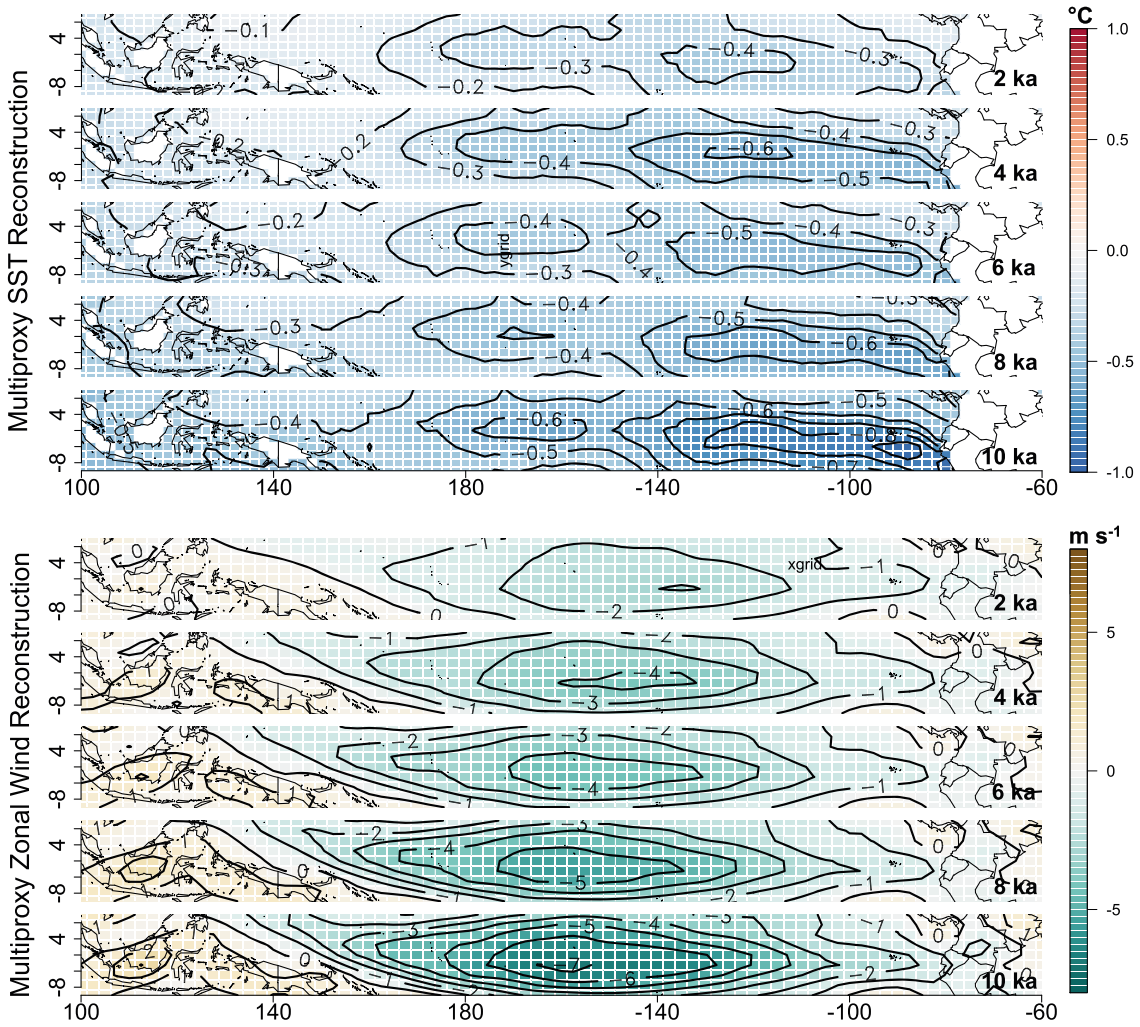

Figure 6. Multiproxy reconstructed (top) equatorial Pacific SST and (bottom) zonal wind anomalies for 10, 8, 6, 4, and 2 ka.

cold anomalies recorded for the early Holocene by records #33 and #29 are due to local coastal upwelling. However, the other two coastal records (#37 and #39) reveal smaller early Holocene cold anomalies and better RSS fits with the reconstructed mean state. For the western Pacific (Figure 8), the highest RSS values are observed on proxies #13 (Mg/Ca, RSS = 26.06°C^2) and #11 (Mg/Ca, RSS = 10.63°C^2). Once again, these two records claim the greatest anomalies during the early Holocene (more negative than −1.5°C), which are not supported by the remaining records in the western Pacific.

The differences between our reconstructions based on Mg/Ca, $U^{k'}_{37}$, or both emphasize the need to gather more paleo observations. If each proxy is subject to seasonal biases, then there is an argument for combining them to get the most complete picture of annual average conditions [*Leduc et al.*, 2010; *Timmermann et al.*, 2014]. The current distribution of proxy records, however, is uneven, with the eastern cold tongue dominated by $U^{k'}_{37}$ and the western warm pool dominated by Mg/Ca. This asymmetry may be acceptable if the two proxies are least biased in those respective regions, as suggested by *Timmermann et al.* [2014], but it is important to note that the EOF1 weightings of equatorial Pacific locations are much larger in the east than in the west (Figure A1). Since there are fewer Mg/Ca records available from the east, imprecisions in those records may lead to greater errors in the Mg/Ca-based reconstructions. First, EOF patterns of SSTs throughout the equatorial Pacific (Figure A1) reveal important regions for future core retrieval, in that high EOF1 values indicate the importance of that particular location in terms of defining the full field variance. Consequently, we suggest that additional Mg/Ca records from the cold tongue region (extending into the central equatorial Pacific to

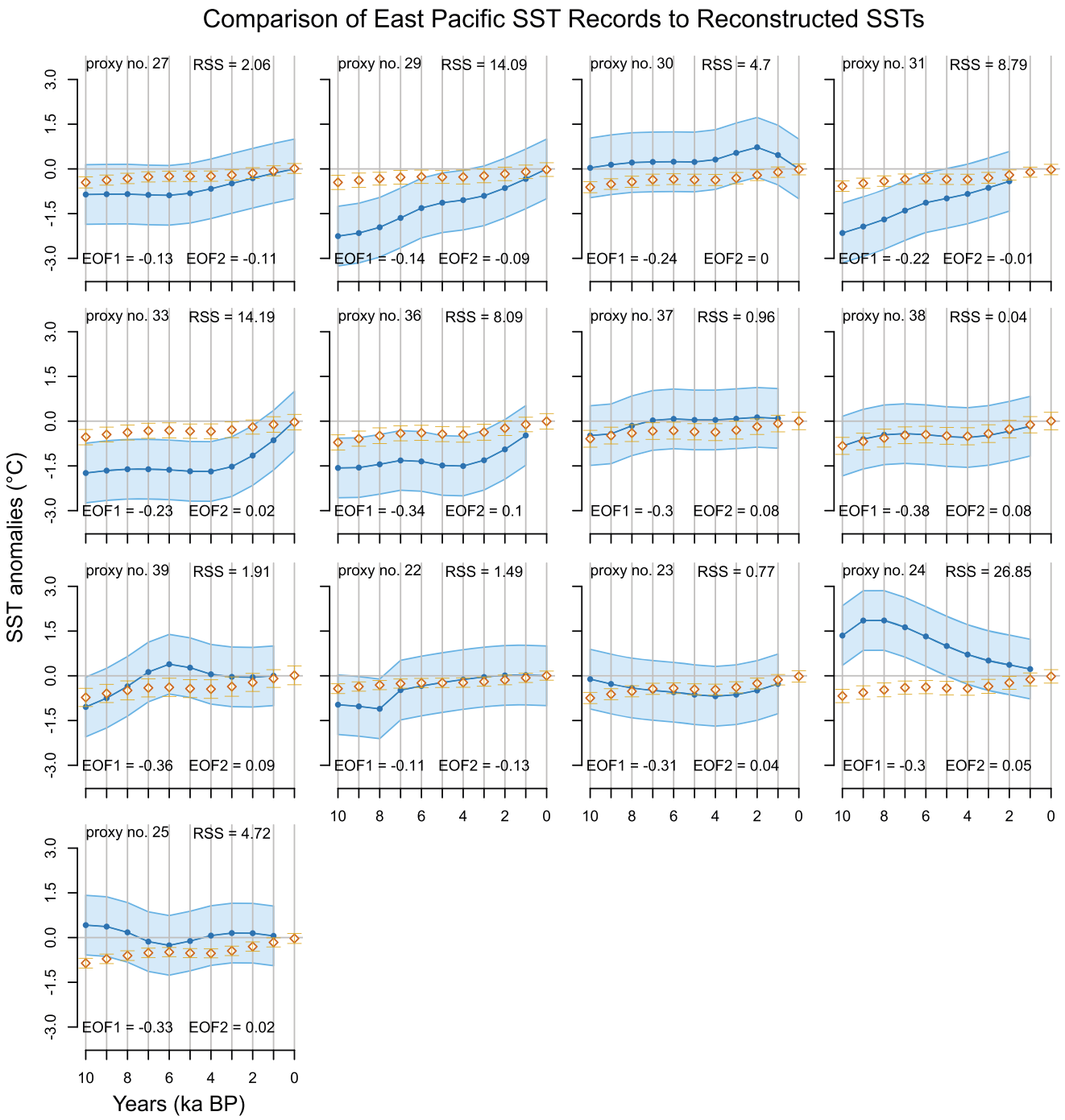

Figure 7. Scatterplots of each proxy record from the eastern Pacific (blue) along with the multiproxy reconstructed SST values for the grid point nearest each record (orange). A nominal error value of ± 1°C is shaded in light blue around each proxy record. Standard errors from the reconstructed model are plotted as orange whiskers. Proxy numbers in the upper left correspond to the numbers in Tables 1 and 2 and Figures 1 and 2. The residual sum of squares is provided to quantify how closely the reconstructed SSTs match the proxy SSTs. As the first two modes of the limited field were used as predictors for the PCA-based reconstruction model, we list the first two eigenvector values at each location on the lower part of each scatterplot. The only records shown here are the ones that were used in the reconstruction. Please refer to Tables 1 and 2 for details on which records were omitted and why.

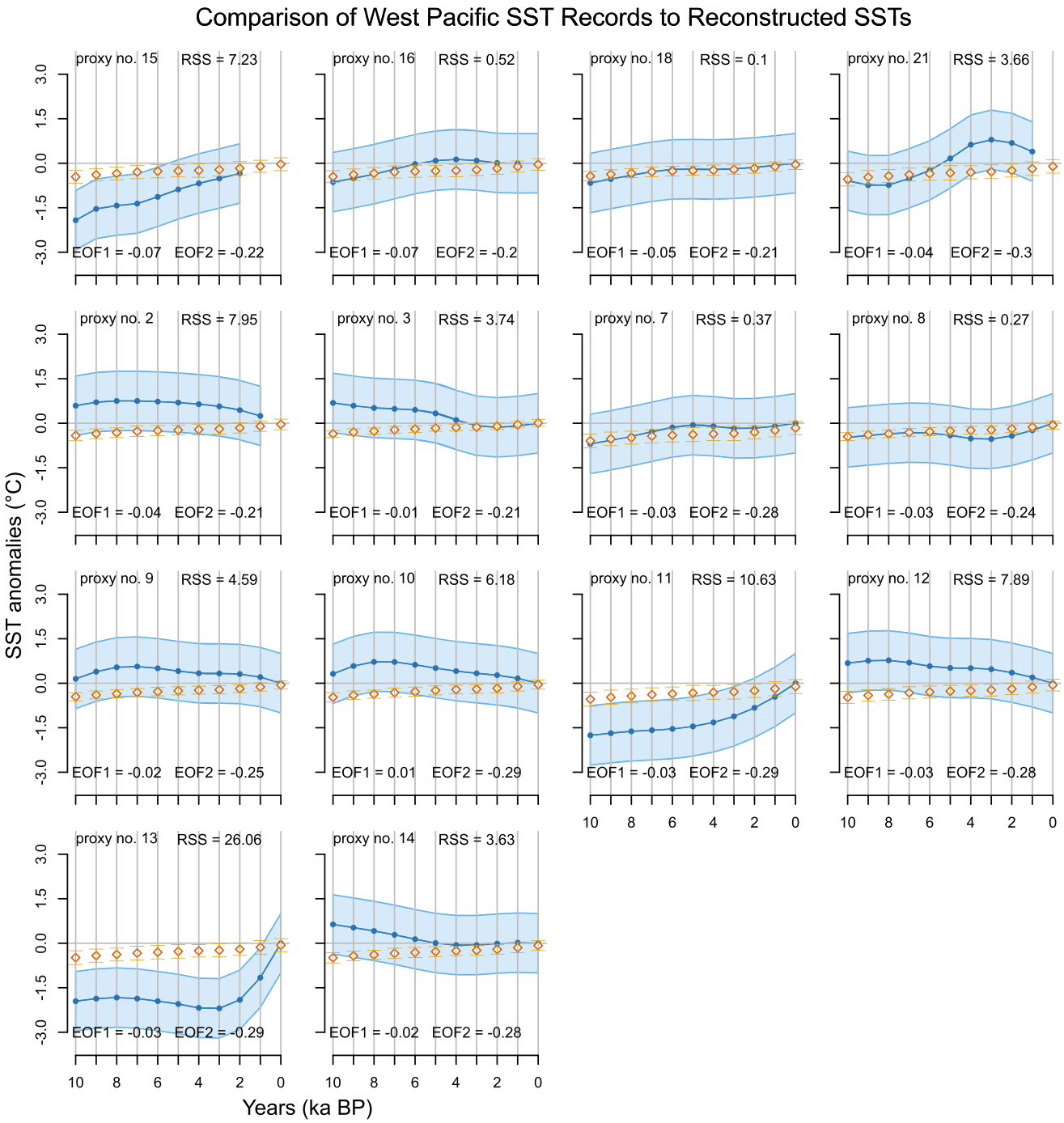

Figure 8. Same as Figure 6 but for western Pacific records.

the extent that is possible) would not only balance representation between the two proxies but also provide information for a critical region of equatorial Pacific variance.

5. Discussion and Conclusions

We apply a PCA-based reduced-dimension procedure to reconstruct full field equatorial Pacific SSTs using networks of Mg/Ca and $U^{k'}_{37}$ records separately, and in combination, for the past 10 ka. For the multiproxy reconstruction, we use a CCA-based approach to reconstruct zonal wind anomalies over the same time period. Major differences in timing and magnitude of SST trends exist when comparing Mg/Ca- and $U^{k'}_{37}$-only SST

reconstructions. Mg/Ca exhibits the greatest eastern cooling and largest zonal difference at 6 ka, consistent with previous Mg/Ca-based inferences [*Koutavas and Joanides*, 2012]. $U^{k'}_{37}$ in contrast, shows the largest anomalies at 10 ka with a gradual relaxation toward modern conditions. The multiproxy approach offers a potential solution to using all possible data despite interproxy discrepancies. A limited spatial field of 27 locations provides enough data to resolve the major patterns of variability for the entire Pacific SSTs and most of the central Pacific zonal winds. For the multiproxy reconstruction, the period with the greatest eastern equatorial Pacific SST anomaly (cooler by 0.9°C) and largest easterly wind anomaly (stronger easterlies by 7 m s^{-1} across the central Pacific) occurred at 10 ka, with similar patterns, but gradually decreasing magnitudes, persisting until 6 ka. By 2 ka, the Pacific remained in a state cooler than present but with SST anomalies around −0.2 to −0.4°C.

The results of a few modeling studies have generated two potential mechanisms to explain cooler equatorial Pacific SSTs during the early Holocene. In one, teleconnections from an enhanced south Asian summer monsoon, due to greater early Holocene summer insolation there, increased Pacific easterly trade winds and facilitated eastern equatorial Pacific upwelling [*Liu et al.*, 2000; *Zheng et al.*, 2008]. In the other, greater insolation over the tropical Pacific in summer enhanced the zonal asymmetry in atmospheric heating and created stronger easterlies [*Bush*, 1999; *Clement et al.*, 1999, 2000]. The results of these studies for the mid-Holocene suggest a range of SST anomalies from −0.5°C [*Clement et al.*, 2000; *Liu et al.*, 2000] up to −1°C [*Bush*, 1999], whereas both our Mg/Ca and $U^{k'}_{37}$ SST reconstructions suggest anomalies closer to −0.8°C, rendering us unable to determine whether one proxy is more consistent with a certain mechanism over the other. Moreover, seasonal differences in SSTs calculated by both *Clement et al.* [2000] and *Liu et al.* [2000] are sufficiently similar that even if Mg/Ca and $U^{k'}_{37}$ SST reconstructions could be associated with different seasons, they would not distinguish between these mechanisms.

Some studies have suggested that increasing greenhouse gases may increase the frequency of ENSO events, and thus make the average SST of the eastern Pacific warmer [*Timmermann et al.*, 1999], but possibly not until CO_2 levels reach four times preindustrial values [*Collins*, 2000]. A recent reconstruction of ice cores intended to constrain CO_2 levels over the past 24 ka [*Schmitt et al.*, 2012] shows that early Holocene CO_2 levels were only slightly lower, by 20 ppm, than those at 2 ka. Given the insignificant effect of CO_2 on present day ENSO [e.g., *Collins*, 2000; *Collins et al.*, 2010], we do not expect greenhouse gases to have played a role in the warming trend from 10 to 2 ka shown in our reconstructions.

An enhanced mean zonal SST gradient with stronger easterlies is likely to have suppressed the growth of El Niño events [*Clement et al.*, 1999; *Otto-Bliesner et al.*, 2003; *Zheng et al.*, 2008]. *Sadekov et al.* [2013] claimed that paleoclimate reconstructions support a strong relationship between ENSO variability and the equatorial Pacific mean state, in that as the zonal gradient increases (a La Niña-like SST distribution), ENSO variability decreases. Various reconstructions provide evidence for reduced ENSO variability during the early to mid-Holocene but with differences in timing among archives. Those that support a continuous increase of ENSO variability since the early Holocene [e.g., *Moy et al.*, 2002; *Rodbell et al.*, 1999] and the model calculations of *Clement et al.* [2000] are most consistent with our $U^{k'}_{37}$ and multiproxy reconstructions, but those that show lowest variability during the mid-Holocene [e.g., *Carré et al.*, 2014; *Koutavas et al.*, 2006; *Koutavas and Joanides*, 2012] are better aligned with our Mg/Ca-based reconstructions. An alternative, based on compiled coral and mollusk archives, is that much of the Holocene was in a reduced ENSO state [*Cobb et al.*, 2013; *Emile-Geay et al.*, 2015], which is broadly consistent with all of our reconstructions in that every 2 kyr interval is colder than modern and with larger zonal SST differences.

Appendix A: Detailed Description of Reconstruction Methods

This appendix provides details on the PCA and CCA reconstruction methods used in the paper, which are also outlined in a schematic (Figure 3). We use bold-faced uppercase variables to denote matrices, with brackets used only when specifying the dimensions of the matrix, and lowercase bold-faced variables to denote vectors.

A1. Principal Component Analysis (PCA) Reconstruction for SSTs

Step A1.1. Let $\boldsymbol{T}$ be an $N \times P$ matrix of contemporary average annual (May–April) SST anomalies composed of (N =) 160 years of data (1854–2014) at each of (G =) 973 grid points spanning the equatorial Pacific from 10°S to 10°N and 100°E to 75°W (285°E). A PCA is performed on $\boldsymbol{T}$, such that

$$[\boldsymbol{T}]_{N\times G} = [\boldsymbol{Y}]_{N\times G}[\boldsymbol{U}]_{G\times G} \tag{A1}$$

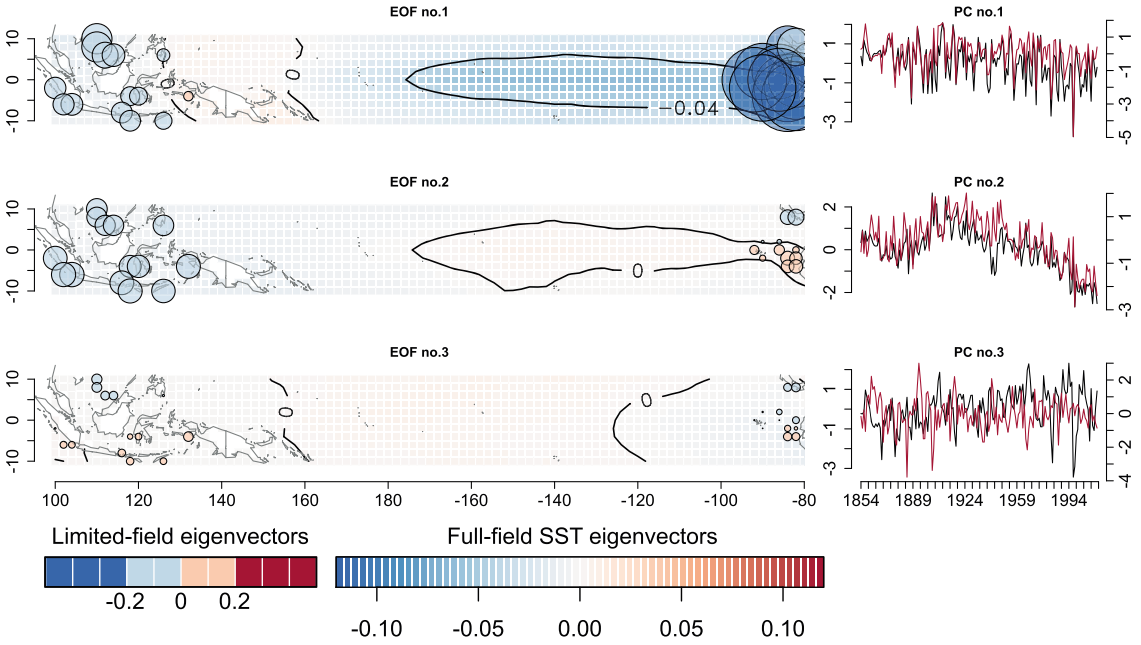

Figure A1. EOFs (shaded) and normalized PCs (black time series) of the three leading modes of the PCA performed on the full field of equatorial Pacific annual averaged (May to April) SSTs obtained from the 1854–2013 2° × 2° ERSST data set [*Smith et al.*, 2008]. Limited SST field EOFs (circles, whose areas are scaled to eigenvalues) and normalized PCs (red time series) are plotted on top of the full field modes. All EOFs are multiplied by their respective eigenvalue (percentage of variance explained by that mode) to show relative strengths across subsequent modes. The first three eigenvalues of the full field PCA were $\lambda_1 = 0.688$, $\lambda_2 = 0.111$, and $\lambda_3 = 0.071$. The first two eigenvalues of the limited field PCA were $\lambda_1^\dagger = 0.799$ and $\lambda_2^\dagger = 0.119$.

$$\boldsymbol{T} = \sum_{i=1}^{G} \lambda_i \boldsymbol{y}_i \boldsymbol{u}_i \tag{A2}$$

whereby $\boldsymbol{T}$ is decomposed into G orthogonal modes. For each ith mode, we find a G-vector empirical orthogonal function (EOF) represented by $\boldsymbol{u}_i$ and an N-vector principal component (PC) represented by $\boldsymbol{y}_i$, which respectively describe the spatial and temporal variability of that particular eigenvector. In addition, λ_i is a scalar equal to the fraction of total variance of the original data that is resolved by the ith mode. The first three EOFs (Figure A1, left) and PCs (Figure A1, right) explain almost 90% of the total variance of the full field SST data ($\lambda_1 = 0.688$, $\lambda_2 = 0.111$, and $\lambda_3 = 0.071$).

Step A1.2. Let $\boldsymbol{T}^\dagger$ be a matrix of contemporary SST anomalies at the locations for which we have proxy records (referred to as the "limited field" hereafter), which makes it order $N \times P$, where N is again 160 (years) and P is 27 (proxy sites). A PCA is performed on $\boldsymbol{T}^\dagger$, which similarly results in P orthogonal modes, each with a P-vector EOF, $\boldsymbol{u}_i^\dagger$, N-vector $\boldsymbol{y}_i^\dagger$, and scalar $\lambda_i^\dagger$.

$$[\boldsymbol{T}^\dagger]_{N\times P} = [\boldsymbol{Y}^\dagger]_{N\times P}[\boldsymbol{U}^\dagger]_{P\times P} \tag{A3}$$

$$\boldsymbol{T}^\dagger = \sum_{i=1}^{P} \lambda_i^\dagger \boldsymbol{y}_i^\dagger \boldsymbol{u}_i^\dagger \tag{A4}$$

The first two modes (Figure A1) explain 92% of the total variance of the limited field SST data ($\lambda_1^\dagger = 0.799$, and $\lambda_2^\dagger = 0.119$).

Step A1.3. We performed the following steps for each of six reconstruction periods: 2, 4, 6, 8, and 10 ka. It should be noted that although Tables 1 and 2 list information for 39 independent proxy records, only 27 were used in the multiproxy reconstruction. As noted in each table, 12 records were discarded from the reconstruction because each one either (1) did not extend to 2 ka B.P., in which case we could not justify smoothing the records to 0 ka, or (2) snapped to the same gridcell as another proxy record of higher resolution. Using the smoothed proxy records, all 27 estimates of SST for, say, 10 ka are contained in matrix $\boldsymbol{R}$ of order 1 by P,

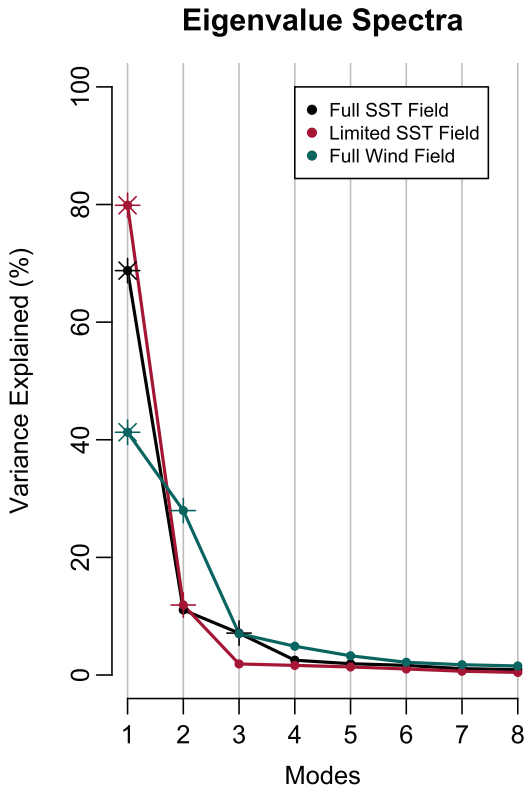

Figure A2. Eigenvalue spectra (EVS) for the (a) full SST field (1854–2013; black), (b) limited SST field (1854–2013; red), and (c) full zonal wind field (1949–2013; green). The limited SST field consists of contemporary SSTs only at locations for which there exists either Mg/Ca or $U^{k'}_{37}$ SST records. Asterisks represent the variance explained by the first mode of each field. The plus signs represent the variance explained at the "knee," which is the point just before the noise floor (represented by small points). Description of how these are used to determine the number of retained PCs and predictors used in the model is provided in the Appendix.

where $P = 27$. Eigenvalue decomposition of $\boldsymbol{R}$ is accomplished by multiplying it by the eigenvalue transformation matrix $\boldsymbol{U}^{\dagger}$ obtained from the limited field PCA in Step A1.2:

$$[\boldsymbol{Y}^{R}]_{1\times P} = [\boldsymbol{R}]_{1\times P}[\boldsymbol{U}^{\dagger}]^{T}_{P\times P} \tag{A5}$$

where $\boldsymbol{Y}^{R}$ represents the PCs of the proxy SST values for 10 ka.

Step A1.4. For the reconstruction model, we use a few of the PCs of the limited field as predictors to model each of the first few full-field PCs. The decision to keep a certain number of PCs and predictors is somewhat arbitrary but depends on the distribution of variance resolved across the modes. Although keeping more modes may increase the total resolved variance, inclusion of too many PCs can introduce noise into the calculated fields. Given the eigenvalue spectrum (EVS) of the full-field and limited-field λ values (Figure A2), we were faced with a few reasonable options in deciding how many limited-field predictor PCs to use and how many full-field PCSs to reconstruct. First, we could limit the reconstruction to only the dominant mode or the first PC (represented by the asterisk on Figure A2). In this case, we would model the first PC of the full field as a function of the first PC of the limited field. As a second option, we could choose some percentage of resolved variance as a threshold. If we choose PCs that resolve 10% or more of the variance, we would model the first two PCs of the full field each as functions of the first two PCs of the limited field. If we chose 5% as a threshold, the number of predictors would remain the same, but we would now model the first three PCs of the full field. A final option would be to use the "knee" in the eigenvalue spectra as thresholds (plus signs in Figure A2). The knee of each EVS is located at the PC just before each noise floor (small points in Figure A2). Coincidentally, it turns out that using either 5% or the knee as a threshold achieves the same combination of PCs (first three) and predictor PCs (first two). Reconstructions of SSTs for each of these three scenarios were considered. Using only the first PC of each did not reconstruct modern day SSTs well enough because it omitted other important non-noise

modes. Although the second (10% threshold) and third (5% threshold or knee) scenarios reconstructed both modern day and Holocene SSTs similarly, we chose to use the latter to include the most possible PCs.

With this reasoning in mind, we model the first three PCs of the full field each as a linear function of the first two PCs of the limited field:

$$\begin{aligned} \boldsymbol{y}_1 &= f(\boldsymbol{y}_1^\dagger, \boldsymbol{y}_2^\dagger) \\ \boldsymbol{y}_2 &= f(\boldsymbol{y}_1^\dagger, \boldsymbol{y}_2^\dagger) \\ \boldsymbol{y}_3 &= f(\boldsymbol{y}_1^\dagger, \boldsymbol{y}_2^\dagger) \end{aligned} \tag{A6}$$

The best linear regression model for each is identified via stepwise model selection based on Bayesian Information Criterion (BIC). BIC is calculated by BIC $= -2[\text{loglikelihood}] + d[\log(N)]$, where N is the sample size and d is the total number of parameters used to fit each model. Lower BIC indicates better model performance.

Step A1.5. We use the PCs of the proxy data $\boldsymbol{Y}^R$ to reconstruct the first three PCs representative of 10 ka ($\hat{\boldsymbol{y}}_1$, $\hat{\boldsymbol{y}}_2$, $\hat{\boldsymbol{y}}_3$) and similarly for other times. The remaining G minus 3 reconstructed PCs ($\hat{\boldsymbol{y}}_{4\ldots G}$) are the means of the PCs from the full field ($\boldsymbol{y}_{4\ldots G}$).

We use the PCs of the proxy data $\boldsymbol{Y}^R$ to reconstruct the first three PCs representative of full field SSTs at 10 ka ($\hat{\boldsymbol{y}}_1$, $\hat{\boldsymbol{y}}_2$, $\hat{\boldsymbol{y}}_3$), and similarly for other times. Recall, however, that there were G PCs for the full field. To obtain the remaining reconstructed PCs ($\hat{\boldsymbol{y}}_{4\ldots G}$), we take the means of the PCs from the full field ($\boldsymbol{y}_{4\ldots G}$).

Step A1.6. Finally, we transform the reconstructed PCs into a field of reconstructed SST anomalies via eigenvalue expansion, by multiplying by the original eigenvalue matrix from Step A1.1:

$$[\hat{\boldsymbol{T}}]_{1\times G} = [\hat{\boldsymbol{Y}}]_{1\times G}[\boldsymbol{U}]_{G\times G} \tag{A7}$$

Since $\hat{\boldsymbol{T}}$ is estimated using only the first few PCs, the reconstructed SSTs represent only the dominant signal. Steps A1.1 – A1.6 are repeated for 8, 6, 4, and 2 ka.

Standard errors from the regressions in Step A1.4 are used to generate 500 ensembles of the first three PCs. Five hundred ensembles for each of the remaining PCs were created by bootstrapping values from the original PCs at each grid point. The standard deviation of these ensembles provides an estimate of uncertainty. Standard errors are generally between 0.1 and 0.2°C throughout the central Pacific, with some errors reaching 0.3°C immediately along the coast of South America. Present-day variance is concentrated in the cold tongue of the eastern and east-central Pacific. In most places, the standard errors are only a small fraction (<10%) of the present-day variance.

A2. Canonical Correlation Analysis (CCA) Reconstruction of Zonal Winds

For the most part, the CCA method follows the PCA method described in Figure 3 through Steps A1.1 – A1.3 and then differs from Step A1.4 onward. For Steps A1.1 and A1.2, $\boldsymbol{T}$ becomes a matrix of 1949 – 2013 zonal wind anomalies, which we will call $\boldsymbol{Z}$, and $\boldsymbol{T}^\dagger$ remains a matrix of SST anomalies for the limited field. Since we only have 65 years of zonal wind data, N is now 65. As before, a PCA on both of these fields results in

$$[\boldsymbol{Z}]_{N\times G} = [\boldsymbol{Y}]_{N\times G}[\boldsymbol{U}]_{G\times G} \tag{A8}$$

$$[\boldsymbol{T}^\dagger]_{N\times P} = [\boldsymbol{Y}^\dagger]_{N\times P}[\boldsymbol{U}^\dagger]_{P\times P} \tag{A9}$$

where $\boldsymbol{Y}$ and $\boldsymbol{U}$ are the full field PCs and eigenvectors of the zonal winds (Figure A3) and $\boldsymbol{Y}^\dagger$ and $\boldsymbol{U}^\dagger$ are still the limited-field PCs and eigenvectors (Figure A1). Step A1.3 is the same: the proxy data $\boldsymbol{R}$ are decomposed into PCs, $\boldsymbol{Y}^R$, by multiplying by the limited field eigenvalues, $\boldsymbol{U}^\dagger$.

At this point, N_{PC} from $\boldsymbol{Y}$ and $\boldsymbol{Y}^\dagger$ are retained. Note that in a CCA the numbers of full-field and of limited-field PCs retained must be equal. It is also worth noting that since a canonical correlation resolves the joint correlation between two PCs, it is acceptable to retain more PCs than one typically does during a standard PCA reconstruction. In fact, for zonal winds, keeping the first six PCs ($N_{PC} = 6$), which involves keeping PCs below the knee in Figure A2, strengthened the model statistics and allowed us to account for 87% of the full-field variance in monthly mean zonal wind speeds. A canonical correlation is performed between the two to resolve the joint correlation between the two sets of PCs:

$$[\boldsymbol{Y}]_{N\times N_{PC}} = [\boldsymbol{S}]_{N\times N_{PC}}[\boldsymbol{A}]_{N_{PC}\times N_{PC}} \tag{A10}$$

$$[\boldsymbol{Y}^\dagger]_{N\times N_{PC}} = [\boldsymbol{S}^\dagger]_{N\times N_{PC}}[\boldsymbol{B}]_{N_{PC}\times N_{PC}} \tag{A11}$$

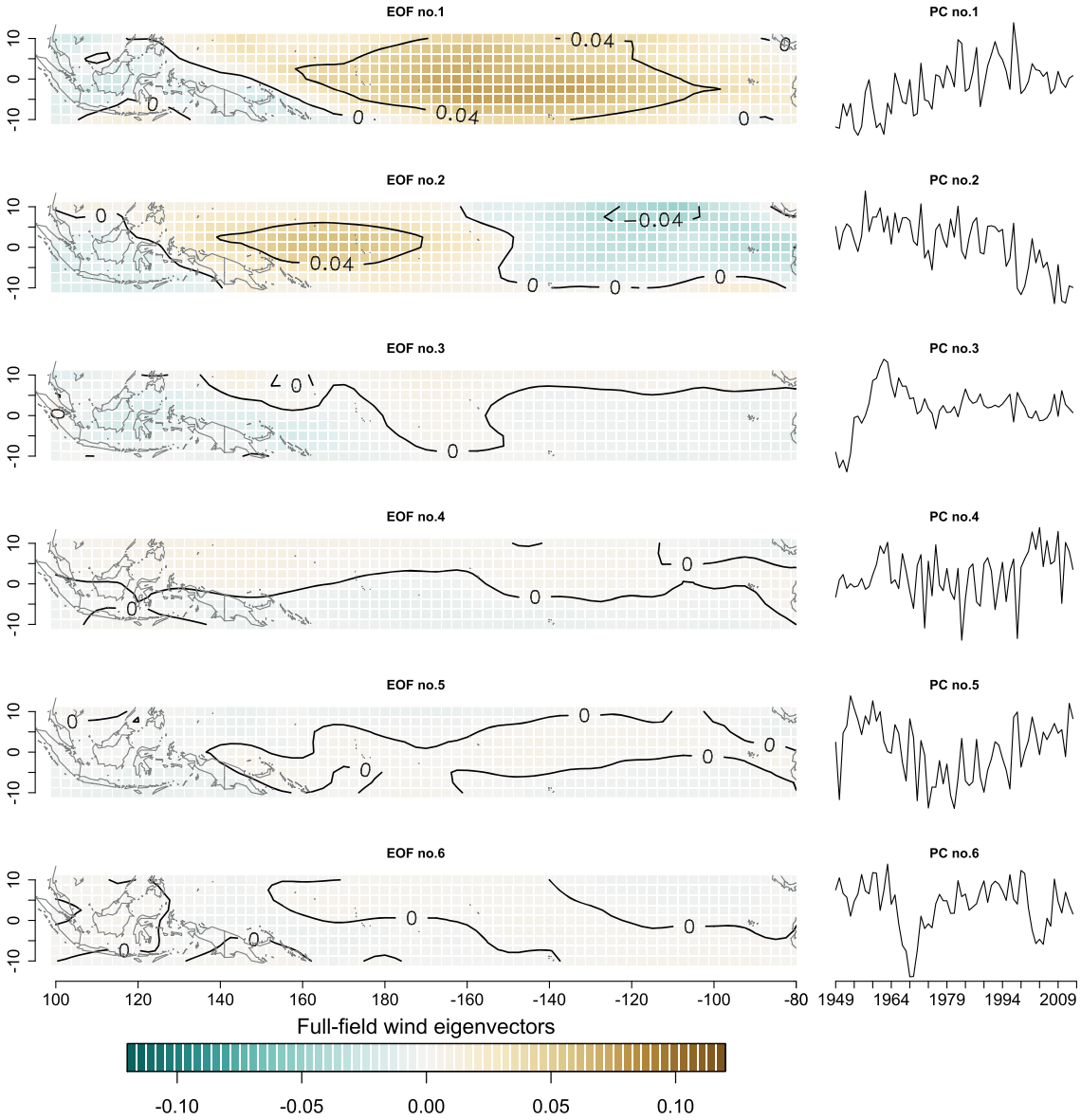

Figure A3. EOFs (shaded) and PCs (black time series) of the six leading modes of the PCA performed on the full field of equatorial Pacific annually averaged (May to April) zonal winds obtained from the 1949–2013 2.5° × 2.5° NCEP-NCAR Reanalysis [*Kalnay et al.*, 1996]. As with Figure A1, EOFs are multiplied by their respective eigenvalue ($\lambda_1 = 0.413$, $\lambda_2 = 0.280$, $\lambda_3 = 0.070$, $\lambda_4 = 0.049$, $\lambda_5 = 0.033$, and $\lambda_6 = 0.022$).

where $\boldsymbol{A}$ and $\boldsymbol{B}$ are now the canonical transformation functions, $\boldsymbol{S}$ and $\boldsymbol{S}^{\dagger}$ are N_{PC} pairs of canonical components (CCs), each of which explains more of the joint variance than the next, and all of which are uncorrelated to each other. The CC of the full field are regressed against the corresponding CC of the limited field, such that

$$s_j = \hat{a}_j + \beta_j s_j^{\dagger} \tag{A12}$$

where j is 1 through N_{PC}, and $\hat{\boldsymbol{\beta}}$ is the solution to the least squares optimization. The first N_{PC} reconstructed PCs of the full wind field $\hat{\boldsymbol{Y}}$ are obtained through expansion by multiplication of first N_{PC} proxy PCs with the full-field canonical transformation matrix $\boldsymbol{A}$ and the $\hat{\boldsymbol{\beta}}$ solution to the regression:

$$[\hat{\boldsymbol{Y}}]_{1\times N_{PC}} = [\boldsymbol{Y}^{R}]_{1\times N_{PC}}[\boldsymbol{A}]_{N_{PC}\times N_{PC}}[\hat{\boldsymbol{\beta}}]_{N_{PC}\times N_{PC}} \tag{A13}$$

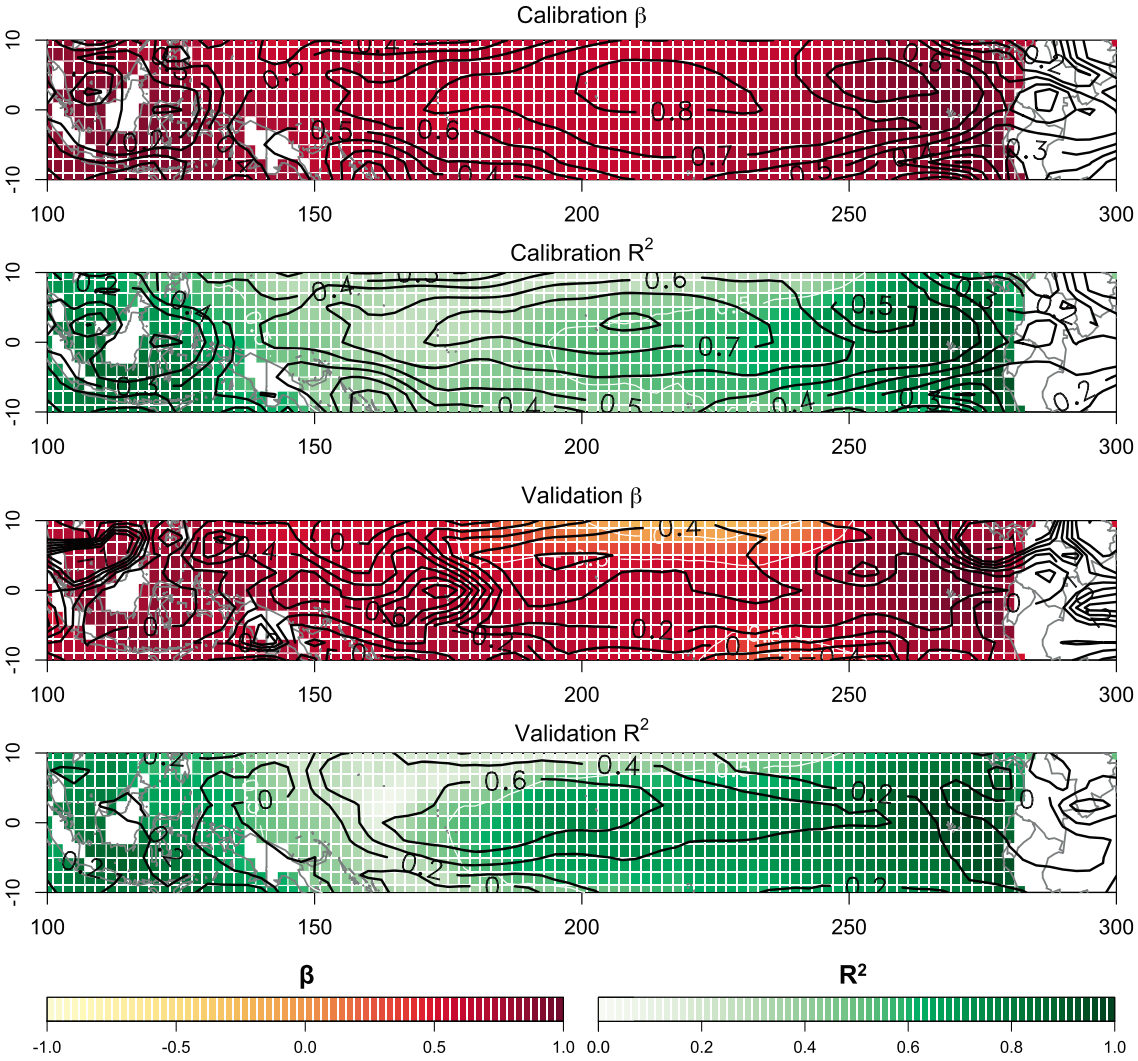

Figure A4. Model calibration statistics for the PCA-based SST model (shading and white contours) and the CCA-based zonal wind model (black contours) showing the skill of the models in reconstructing each contemporary data set (1854–2013 for SSTs and 1949–2013 for zonal winds). The β statistic represents the resolved variance captured by the reconstructed contemporary data. The R^2 equals the square of the correlation between the observed contemporary data and the reconstructed contemporary data. Model validation was performed by training the model on 1980–2013 data and using that model to validate SSTs and zonal winds from the period prior (1854–1979 for SSTs and 1949–1979 for zonal winds). The β and R^2 statistics are used once again to quantify model skill.

We calculate the remaining G minus N_{PC} PCs ($\hat{y}_{7\ldots G}$) by taking the means of the PCs from the full field. Finally, we obtain the reconstructed zonal winds $\hat{\boldsymbol{Z}}$ by eigenvalue expansion:

$$[\hat{\boldsymbol{Z}}]_{1\times G} = [\hat{\boldsymbol{Y}}]_{1\times G}[\boldsymbol{U}]_{G\times G} \tag{A14}$$

We repeated this process for each of the five time periods (10, 8, 6, 4, and 2 ka).

A3. Calibration and Validation of the Model Using β and R^2 Statistics

To assess the reliability of the procedure described above to reproduce contemporary SSTs and zonal winds from the limited field contemporary SST data, we use two criteria. First is the "resolved variance" statistic β, given by

$$\beta = 1 - \frac{\sum (y - \hat{y})^2}{\sum y^2} \tag{A15}$$

where y is the contemporary data and $\hat{y}$ is the reconstructed data for the full period of each data set (1854–2014 for SST and 1949–2013 for winds). We compute this statistic at each grid point over the reconstruction domain (Figure A4, "Calibration β"). For a perfect fit, one would expect $\beta = 1$, and for two random

series, one would expect $\beta = -1$. Across most of the reconstruction region, β is greater than 0.6 for both SSTs (shaded) and zonal winds (black contours). The lowest β values are found over the central Pacific for SSTs and over the landmasses in the west and east Pacific for zonal winds.

We also correlated data and calculated values at each grid point and plot maps of the squared correlation coefficient, R^2 (Figure A4, "Calibration R^2"). For SSTs, the east and west Pacific show the highest correlations, which we should expect, as those areas provide the SST data for the reconstruction. The western cold tongue region of the east-central Pacific, where there are no data, shows values of R^2 greater than or equal to 0.5. The lowest correlation region for SSTs is the west-central Pacific with values of $R^2 = 0.2-0.3$. For zonal winds, the R^2 values are largest in the central Pacific, which is perhaps not surprising, as the central Pacific winds depend on SSTs at either end of the Pacific. As with the β test, the worst performance for winds is seen over continental landmasses east and west of the Pacific.

For model validation, we train the PCA and CCA models using only the most recent data (1980–2013) and withhold the data from earlier periods (1854–1979 for SST, 1949–1979 for winds). Then, we reconstruct the fields from the earlier epoch using each respective model. As expected, the distribution of β and R^2 statistics (Figure A4, "Validation β" and "Validation R^2") show smaller values than the calibration statistics for the complete data sets, but the regions that were reconstructed best during the calibration experiments match those reconstructed best in the verification test (Figure A4). For SSTs, the training model reconstructs the earlier period everywhere except the west-central Pacific and areas near 10°S and 10°N in the central Pacific. For zonal winds, the central Pacific is the only region that is reconstructed using the training model. These patterns are consistent across both the β and R^2 statistics.

Acknowledgments
This research was supported in part by the National Science Foundation (NSF) through a postdoctoral research fellowship award AGS-PRF-1525465 (to E.C.G.) and under grants EAR-1211378 (to P.M.) and OCE-1103482 (to T.M.M.). This work was also supported by a Cooperative Institute for Research in Environmental Sciences (CIRES) Graduate Student Fellowship during Spring 2015 and CU-Boulder Graduate School Dissertation Completion Funds during Summer 2015. We are grateful for the constructive criticism of three anonymous reviewers and Tim Herbert. We thank Markus Kienast for providing his feedback, his original proxy data, and additional proxy records to consider. Thanks to Andreas Lückge, Robert Thunell, Claire Waelbroeck, and Samantha Bova for providing their original proxy data. Finally, we thank Mark Cane and Yochanan Kushnir for their advice during the early stages of this project. All contemporary data used in this study can be accessed using the IRI Climate Data Library (http://iridl.ldeo.columbia.edu/). All proxy data used in this study can be found in the archives of NCDC (http://www.ncdc.noaa.gov/data-access/paleoclimatology-data/datasets) and Pangaea (http://www.pangaea.de/). All data analysis was done in R [*R Core Team*, 2014].

References

Anand, P., H. Elderfield, and M. H. Conte (2003), Calibration of Mg/Ca thermometry in planktonic foraminifera from a sediment trap time series, *Paleoceanography*, *18*(2), 1050, doi:10.1029/2002PA000846.

Ashkenazy, Y., and E. Tziperman (2006), Scenarios regarding the lead of equatorial sea surface temperature over global ice volume, *Paleoceanography*, *21*, PA2006, doi:10.1029/2005PA001232.

Barnett, T., and R. Preisendorfer (1987), Origins and levels of monthly and seasonal forecast skill for United States surface air temperatures determined by canonical correlation analysis, *Mon. Weather Rev.*, *115*(9), 1825–1850.

Barnston, A. G. (1994), Linear statistical short-term climate predictive skill in the Northern Hemisphere, *J. Clim.*, *7*(10), 1513–1564.

Barnston, A. G., and C. F. Ropelewski (1992), Prediction of ENSO episodes using canonical correlation analysis, *J. Clim.*, *5*(11), 1316–1345.

Barnston, A. G., and T. M. Smith (1996), Specification and prediction of global surface temperature and precipitation from global SST using CCA, *J. Clim.*, *9*(11), 2660–2697.

Benway, H. M., A. C. Mix, B. A. Haley, and G. P. Klinkhammer (2006), Eastern pacific warm pool paleosalinity and climate variability: 0–30 kyr, *Paleoceanography*, *21*, PA3008, doi:10.1029/2005PA001208.

Berger, W., M. Bonneau, and F. Parker (1982), Foraminifera on the deep-sea floor-lysocline and dissolution rate, *Oceanol. Acta*, *5*(2), 249–258.

Bjerknes, J. (1969), Atmospheric teleconnections from the equatorial Pacific, *Mon. Weather Rev.*, *97*(3), 163–172.

Bolliet, T., A. Holbourn, W. Kuhnt, C. Laj, C. Kissel, L. Beaufort, M. Kienast, N. Andersen, and D. Garbe-Schönberg (2011), Mindanao dome variability over the last 160 kyr: Episodic glacial cooling of the west Pacific warm pool, *Paleoceanography*, *26*, PA1208, doi:10.1029/2010PA001966.

Bova, S. C., T. Herbert, Y. Rosenthal, J. Kalansky, M. Altabet, C. Chazen, A. Mojarro, and J. Zech (2015), Links between eastern equatorial pacific stratification and atmospheric CO_2 rise during the last deglaciation, *Paleoceanography*, *30*, 1407–1424, doi:10.1002/2015PA002816.

Brassell, S., G. Eglinton, I. Marlowe, U. Pflaumann, and M. Sarnthein (1986), Molecular stratigraphy: A new tool for climatic assessment, *Nature*, *320*, 129–133.

Bretherton, C. S., C. Smith, and J. M. Wallace (1992), An intercomparison of methods for finding coupled patterns in climate data, *J. Clim.*, *5*(6), 541–560.

Bush, A. B. (1999), Assessing the impact of mid-Holocene insolation on the atmosphere-ocean system, *Geophys. Res. Lett.*, *26*(1), 99–102.

Carré, M., J. P. Sachs, S. Purca, A. J. Schauer, P. Braconnot, R. A. Falcón, M. Julien, and D. Lavallée (2014), Holocene history of ENSO variance and asymmetry in the eastern tropical pacific, *Science*, *345*(6200), 1045–1048.

Chen, Y.-l. L., H.-Y. Chen, and C.-W. Chung (2007), Seasonal variability of coccolithophore abundance and assemblage in the northern South China Sea, *Deep Sea Res., Part II*, *54*(14), 1617–1633.

Cherry, S. (1996), Singular value decomposition analysis and canonical correlation analysis, *J. Clim.*, *9*(9), 2003–2009.

Clement, A., R. Seager, and M. Cane (1999), Orbital controls on the El Niño/Southern Oscillation and the tropical climate, *Paleoceanography*, *14*(4), 441–456.

Clement, A. C., R. Seager, and M. A. Cane (2000), Suppression of El Niño during the mid-holocene by changes in the Earth's orbit, *Paleoceanography*, *15*(6), 731–737.

Cobb, K. M., N. Westphal, H. R. Sayani, J. T. Watson, E. Di Lorenzo, H. Cheng, R. Edwards, and C. D. Charles (2013), Highly variable El Niño–Southern Oscillation throughout the holocene, *Science*, *339*(6115), 67–70.

Collins, M. (2000), The El Niño–Southern Oscillation in the second Hadley centre coupled model and its response to greenhouse warming, *J. Clim.*, *13*(7), 1299–1312.

Collins, M., et al. (2010), The impact of global warming on the tropical Pacific Ocean and El Niño, *Nat. Geosci.*, *3*(6), 391–397.

Conte, M. H., M.-A. Sicre, C. Rühlemann, J. C. Weber, S. Schulte, D. Schulz-Bull, and T. Blanz (2006), Global temperature calibration of the alkenone unsaturation index ($U^{K'}_{37}$) in surface waters and comparison with surface sediments, *Geochem. Geophys. Geosyst.*, *7*, Q02005, doi:10.1029/2005GC001054.

Cook, E. R., D. M. Meko, D. W. Stahle, and M. K. Cleaveland (1999), Drought reconstructions for the Continental United States*, *J. Clim.*, *12*(4), 1145–1162.
de Garidel-Thoron, T., Y. Rosenthal, F. Bassinot, and L. Beaufort (2005), Stable sea surface temperatures in the Western Pacific warm pool over the past 1.75 million years, *Nature*, *433*(7023), 294–298.
de Garidel-Thoron, T., Y. Rosenthal, L. Beaufort, E. Bard, C. Sonzogni, and A. C. Mix (2007), A multiproxy assessment of the western equatorial Pacific hydrography during the last 30 kyr, *Paleoceanography*, *22*, PA3204, doi:10.1029/2006PA001269.
Dekens, P. S., D. W. Lea, D. K. Pak, and H. J. Spero (2002), Core top calibration of mg/ca in tropical foraminifera: Refining paleotemperature estimation, *Geochem. Geophys. Geosyst.*, *3*(4), 1–29, doi:10.1029/2001GC000200.
Dickson, A., and F. Millero (1987), A comparison of the equilibrium constants for the dissociation of carbonic acid in seawater media, *Deep Sea Res. Part A*, *34*(10), 1733–1743.
Dubois, N., M. Kienast, C. Normandeau, and T. D. Herbert (2009), Eastern equatorial Pacific cold tongue during the Last Glacial Maximum as seen from alkenone paleothermometry, *Paleoceanography*, *24*, PA4207, doi:10.1029/2009PA001781.
Emile-Geay, J., K. M. Cobb, M. E. Mann, and A. T. Wittenberg (2013), Estimating central equatorial Pacific SST variability over the past millennium. Part II: Reconstructions and implications, *J. Clim.*, *26*(7), 2329–2352.
Emile-Geay, J., et al. (2015), Links between tropical pacific seasonal, interannual and orbital variability during the Holocene, *Nat. Geosci.*, *9*, 168–173.
Evans, M. N., A. Kaplan, and M. A. Cane (2002), Pacific sea surface temperature field reconstruction from coral δ18O data using reduced space objective analysis, *Paleoceanography*, *17*(1), 1007, doi:10.1029/2000PA000590.
Fraser, N., W. Kuhnt, A. Holbourn, T. Bolliet, N. Andersen, T. Blanz, and L. Beaufort (2014), Precipitation variability within the west Pacific Warm Pool over the past 120 ka: Evidence from the Davao Gulf, southern Philippines, *Paleoceanography*, *29*, 1094–1110, doi:10.1002/2013PA002599.
Harada, N., N. Handa, K. Harada, and H. Matsuoka (2001), Alkenones and particulate fluxes in sediment traps from the central equatorial Pacific, *Deep Sea Res., Part I*, *48*(3), 891–907.
Hastings, D., M. Kienast, S. Steinke, and A. Whitko (2001), A comparison of three independent paleotemperature estimates from a high resolution record of deglacial SST records in the tropical South China Sea, *Eos Trans. AGU*, *1*(10), Fall Meet. Suppl., Abstract #PP12B–10.
Haug, G. H., et al. (2005), North Pacific seasonality and the glaciation of North America 2.7 million years ago, *Nature*, *433*(7028), 821–825.
Herbert, T. D. (2003), Alkenone paleotemperature determinations, in *Treatise on Geochemistry*, vol. 6, p. 625, Elsevier, doi:10.1016/B0-08-043751-6/06115-6.
Kalnay, E., et al. (1996), The NCEP/NCAR 40-year reanalysis project, *Bull. Am. Meteorol. Soc.*, *77*(3), 437–471.
Kaplan, A., M. A. Cane, Y. Kushnir, A. C. Clement, M. B. Blumenthal, and B. Rajagopalan (1998), Analyses of global sea surface temperature 1856–1991, *J. Geophys. Res.*, *103*(C9), 18,567–18,589.
Kaufman, D. S., et al. (2009), Recent warming reverses long-term Arctic cooling, *Science*, *325*(5945), 1236–1239.
Kienast, M., S. Steinke, K. Stattegger, and S. Calvert (2001), Synchronous tropical South China Sea SST change and Greenland warming during deglaciation, *Science*, *291*(5511), 2132–2134.
Kienast, M., S. S. Kienast, S. E. Calvert, T. I. Eglinton, G. Mollenhauer, R. François, and A. C. Mix (2006), Eastern Pacific cooling and Atlantic overturning circulation during the last deglaciation, *Nature*, *443*(7113), 846–849.
Koutavas, A., and S. Joanides (2012), El Niño–Southern Oscillation extrema in the Holocene and Last Glacial Maximum, *Paleoceanography*, *27*, PA4208, doi:10.1029/2012PA002378.
Koutavas, A., and J. P. Sachs (2008), Northern timing of deglaciation in the eastern equatorial Pacific from alkenone paleothermometry, *Paleoceanography*, *23*, PA4205, doi:10.1029/2008PA001593.
Koutavas, A., J. Lynch-Stieglitz, T. M. Marchitto, and J. P. Sachs (2002), El Nino-like pattern in ice age tropical pacific sea surface temperature, *Science*, *297*(5579), 226–230.
Koutavas, A., et al. (2006), Mid-Holocene El Niño–Southern Oscillation (ENSO) attenuation revealed by individual foraminifera in eastern tropical pacific sediments, *Geology*, *34*(12), 993–996.
Lea, D. W., and P. A. Martin (1996), A rapid mass spectrometric method for the simultaneous analysis of barium, cadmium, and strontium in foraminifera shells, *Geochim. Cosmochim. Acta*, *60*(16), 3143–3149.
Lea, D. W., T. A. Mashiotta, and H. J. Spero (1999), Controls on magnesium and strontium uptake in planktonic foraminifera determined by live culturing, *Geochim. Cosmochim. Acta*, *63*(16), 2369–2379.
Lea, D. W., D. K. Pak, and H. J. Spero (2000), Climate impact of late quaternary equatorial Pacific sea surface temperature variations, *Science*, *289*(5485), 1719–1724.
Lea, D. W., D. K. Pak, C. L. Belanger, H. J. Spero, M. A. Hall, and N. J. Shackleton (2006), Paleoclimate history of Galapagos surface waters over the last 135,000 yr, *Quat. Sci. Rev.*, *25*(11), 1152–1167.
Leduc, G., L. Vidal, K. Tachikawa, F. Rostek, C. Sonzogni, L. Beaufort, and E. Bard (2007), Moisture transport across Central America as a positive feedback on abrupt climatic changes, *Nature*, *445*(7130), 908–911.
Leduc, G., R. Schneider, J.-H. Kim, and G. Lohmann (2010), Holocene and Eemian sea surface temperature trends as revealed by alkenone and Mg/Ca paleothermometry, *Quat. Sci. Rev.*, *29*(7), 989–1004.
Lee, T. C., F. W. Zwiers, and M. Tsao (2008), Evaluation of proxy-based millennial reconstruction methods, *Clim. Dyn.*, *31*(2–3), 263–281.
Levi, C., L. Labeyrie, F. Bassinot, F. Guichard, E. Cortijo, C. Waelbroeck, N. Caillon, J. Duprat, T. de Garidel-Thoron, and H. Elderfield (2007), Low-latitude hydrological cycle and rapid climate changes during the last deglaciation, *Geochem. Geophys. Geosyst.*, *8*, Q05N12, doi:10.1029/2006GC001514.
Lewis, E., and D. W. R. Wallace (1998), Program developed for CO_2 system calculations, ORNL/CDIAC-105, Carbon Dioxide Information Analysis Center, Oak Ridge Natl, Lab., U.S. Dep. of Energy, Oak Ridge, Tenn.
Li, B., D. W. Nychka, and C. M. Ammann (2010), The value of multiproxy reconstruction of past climate, *J. Am. Stat. Assoc.*, *105*(491), 883–895.
Linsley, B. K., Y. Rosenthal, and D. W. Oppo (2010), Holocene evolution of the indonesian throughflow and the Western Pacific Warm Pool, *Nat. Geosci.*, *3*(8), 578–583.
Liu, Z., J. Kutzbach, and L. Wu (2000), Modeling climate shift of El Niño variability in the Holocene, *Geophys. Res. Lett.*, *27*(15), 2265–2268.
Loader, C. R., et al. (1996), Local likelihood density estimation, *Ann. Stat.*, *24*(4), 1602–1618.
Lückge, A., M. Mohtadi, C. Rühlemann, G. Scheeder, A. Vink, L. Reinhardt, and M. Wiedicke (2009), Monsoon versus ocean circulation controls on paleoenvironmental conditions off Southern Sumatra during the past 300,000 years, *Paleoceanography*, *24*, PA1208, doi:10.1029/2008PA001627.
Luterbacher, J., E. Xoplaki, D. Dietrich, R. Rickli, J. Jacobeit, C. Beck, D. Gyalistras, C. Schmutz, and H. Wanner (2002), Reconstruction of sea level pressure fields over the eastern North Atlantic and Europe back to 1500, *Clim. Dyn.*, *18*(7), 545–561.

Luterbacher, J., D. Dietrich, E. Xoplaki, M. Grosjean, and H. Wanner (2004), European seasonal and annual temperature variability, trends, and extremes since 1500, *Science*, *303*(5663), 1499–1503.
Mann, M. E., R. S. Bradley, and M. K. Hughes (1998), Global-scale temperature patterns and climate forcing over the past six centuries, *Nature*, *392*(6678), 779–787.
Mann, M. E., M. A. Cane, S. E. Zebiak, and A. Clement (2005), Volcanic and solar forcing of the tropical pacific over the past 1000 years, *J. Clim.*, *18*(3), 447–456.
Mann, M. E., Z. Zhang, M. K. Hughes, R. S. Bradley, S. K. Miller, S. Rutherford, and F. Ni (2008), Proxy-based reconstructions of hemispheric and global surface temperature variations over the past two millennia, *Proc. Natl. Acad. Sci.*, *105*(36), 13,252–13,257.
Marchitto, T. M., R. Muscheler, J. D. Ortiz, J. D. Carriquiry, and A. van Geen (2010), Dynamical response of the tropical Pacific Ocean to solar forcing during the early Holocene, *Science*, *330*(6009), 1378–1381.
McGregor, H., M. Fischer, M. Gagan, D. Fink, S. Phipps, H. Wong, and C. Woodroffe (2013), A weak El Niño/Southern Oscillation with delayed seasonal growth around 4,300 years ago, *Nat. Geosci.*, *6*(11), 949–953.
Mehrbach, C. (1973), Measurement of the apparent dissociation constants of carbonic acid in seawater at atmospheric pressure, *Limnol. Oceanogr.*, *18*(6), 897–907.
Mekik, F., R. François, and M. Soon (2007), A novel approach to dissolution correction of Mg/Ca-based paleothermometry in the tropical Pacific, *Paleoceanography*, *22*, PA3217, doi:10.1029/2007PA001504.
Mo, K. C. (2003), Ensemble canonical correlation prediction of surface temperature over the United States, *J. Clim.*, *16*(11), 1665–1683.
Moberg, A., D. M. Sonechkin, K. Holmgren, N. M. Datsenko, and W. Karlén (2005), Highly variable Northern Hemisphere temperatures reconstructed from low-and high-resolution proxy data, *Nature*, *433*(7026), 613–617.
Mohtadi, M., S. Steinke, A. Lückge, J. Groeneveld, and E. C. Hathorne (2010), Glacial to holocene surface hydrography of the tropical eastern Indian Ocean, *Earth Planet. Sci. Lett.*, *292*(1), 89–97.
Molnar, P., and M. A. Cane (2002), El Niño's tropical climate and teleconnections as a blueprint for pre-Ice Age climates, *Paleoceanography*, *17*(2), 1021, doi:10.1029/2001PA000663.
Molnar, P., and M. A. Cane (2007), Early pliocene (pre-Ice Age) El Niño-like global climate: Which El Niño?, *Geosphere*, *3*(5), 337–365.
Moy, C. M., G. O. Seltzer, D. T. Rodbell, and D. M. Anderson (2002), Variability of El Niño/Southern Oscillation activity at millennial timescales during the Holocene epoch, *Nature*, *420*(6912), 162–165.
Müller, P. J., G. Kirst, G. Ruhland, I. von Storch, and A. Rosell-Melé (1998), Calibration of the alkenone paleotemperature index $U^{K'}_{37}$ based on core-tops from the eastern South Atlantic and the global ocean (60°N–60°S), *Geochim. Cosmochim. Acta*, *62*(10), 1757–1772.
Nürnberg, D., J. Bijma, and C. Hemleben (1996), Assessing the reliability of magnesium in foraminiferal calcite as a proxy for water mass temperatures, *Geochim. Cosmochim. Acta*, *60*(5), 803–814.
Nürnberg, D., A. Müller, and R. Schneider (2000), Paleo-sea surface temperature calculations in the equatorial east atlantic from Mg/Ca ratios in planktic foraminifera: A comparison to sea surface temperature estimates from $U^{K'}_{37}$, oxygen isotopes, and foraminiferal transfer function, *Paleoceanography*, *15*(1), 124–134.
Ohkouchi, N., K. Kawamura, H. Kawahata, and H. Okada (1999), Depth ranges of alkenone production in the central Pacific Ocean, *Global Biogeochem. Cycles*, *13*(2), 695–704.
Otto-Bliesner, B. L., E. C. Brady, S.-I. Shin, Z. Liu, and C. Shields (2003), Modeling El Niño and its tropical teleconnections during the last glacial-interglacial cycle, *Geophys. Res. Lett.*, *30*(23), 2198, doi:10.1029/2003GL018553.
Pahnke, K., J. P. Sachs, L. Keigwin, A. Timmermann, and S.-P. Xie (2007), Eastern tropical pacific hydrologic changes during the past 27,000 years from D/H ratios in alkenones, *Paleoceanography*, *22*, PA4214, doi:10.1029/2007PA001468.
Pelejero, C., and J. O. Grimalt (1997), The correlation between the $U^{K'}_{37}$ index and sea surface temperatures in the warm boundary: The South China Sea, *Geochim. Cosmochim. Acta*, *61*(22), 4789–4797.
Pelejero, C., et al. (1999), High-resolution U^{K}_{37} temperature reconstructions in the South China Sea over the past 220 kyr, *Paleoceanography*, *14*(2), 224–231.
Pena, L., I. Cacho, P. Ferretti, and M. Hall (2008), El Niño–Southern Oscillation-like variability during glacial terminations and interlatitudinal teleconnections, *Paleoceanography*, *23*, PA3101, doi:10.1029/2008PA001620.
Prahl, F. G., L. A. Muehlhausen, and D. L. Zahnle (1988), Further evaluation of long-chain alkenones as indicators of paleoceanographic conditions, *Geochim. Cosmochim. Acta*, *52*(9), 2303–2310.
R Core Team (2014), *R: A Language and Environment for Statistical Computing*, R Foundation for Statistical Computing, Vienna, Austria.
Rodbell, D. T., G. O. Seltzer, D. M. Anderson, M. B. Abbott, D. B. Enfield, and J. H. Newman (1999), An ~15,000-year record of El Niño-driven alluviation in southwestern Ecuador, *Science*, *283*(5401), 516–520.
Rosell-Melé, A., and F. G. Prahl (2013), Seasonality of $U^{K'}_{37}$ temperature estimates as inferred from sediment trap data, *Quat. Sci. Rev.*, *72*, 128–136.
Rosenthal, Y., and G. P. Lohmann (2002), Accurate estimation of sea surface temperatures using dissolution-corrected calibrations for Mg/Ca paleothermometry, *Paleoceanography*, *17*(3), 1044, doi:10.1029/2001PA000749.
Rosenthal, Y., D. W. Oppo, and B. K. Linsley (2003), The amplitude and phasing of climate change during the last deglaciation in the Sulu Sea, western equatorial Pacific, *Geophys. Res. Lett.*, *30*(8), 1428, doi:10.1029/2002GL016612.
Rutherford, S., M. Mann, T. Osborn, K. Briffa, P. D. Jones, R. Bradley, and M. Hughes (2005), Proxy-based Northern Hemisphere surface temperature reconstructions: Sensitivity to method, predictor network, target season, and target domain, *J. Clim.*, *18*(13), 2308–2329.
Sadekov, A. Y., R. Ganeshram, L. Pichevin, R. Berdin, E. McClymont, H. Elderfield, and A. W. Tudhope (2013), Palaeoclimate reconstructions reveal a strong link between El Niño–Southern Oscillation and tropical pacific mean state, *Nat. Commun.*, *4*, 2692.
Salas, J. D., C. Fu, and B. Rajagopalan (2010), Long-range forecasting of Colorado streamflows based on hydrologic, atmospheric, and oceanic data, *J. Hydrol. Eng.*, *16*, 508–520.
Schmitt, J., et al. (2012), Carbon isotope constraints on the deglacial CO_2 rise from ice cores, *Science*, *336*(6082), 711–714.
Schneider, B., G. Leduc, and W. Park (2010), Disentangling seasonal signals in holocene climate trends by satellite-model-proxy integration, *Paleoceanography*, *25*, PA4217, doi:10.1029/2009PA001893.
Smith, T. M., R. W. Reynolds, T. C. Peterson, and J. Lawrimore (2008), Improvements to NOAA's historical merged land-ocean surface temperature analysis (1880-2006), *J. Clim.*, *21*(10), 2283–2296.
Sonzogni, C., E. Bard, F. Rostek, R. Lafont, A. Rosell-Mele, and G. Eglinton (1997), Core-top calibration of the alkenone index vs sea surface temperature in the Indian Ocean, *Deep Sea Res., Part II*, *44*(6), 1445–1460.
Steinke, S., M. Kienast, J. Groeneveld, L.-C. Lin, M.-T. Chen, and R. Rendle-Bühring (2008), Proxy dependence of the temporal pattern of deglacial warming in the tropical South China Sea: Toward resolving seasonality, *Quat. Sci. Rev.*, *27*(7), 688–700.
Stott, L., K. Cannariato, R. Thunell, G. H. Haug, A. Koutavas, and S. Lund (2004), Decline of surface temperature and salinity in the western tropical Pacific Ocean in the Holocene epoch, *Nature*, *431*(7004), 56–59.

Thirumalai, K., J. W. Partin, C. S. Jackson, and T. M. Quinn (2013), Statistical constraints on El Niño Southern Oscillation reconstructions using individual foraminifera: A sensitivity analysis, *Paleoceanography*, *28*(3), 401–412.
Thunell, R. C., and L. A. Reynolds (1984), Sedimentation of planktonic foraminifera: Seasonal changes in species flux in the Panama basin, *Micropaleontology*, *30*, 243–262.
Timmermann, A., J. Oberhuber, A. Bacher, M. Esch, M. Latif, and E. Roeckner (1999), Increased El Niño frequency in a climate model forced by future greenhouse warming, *Nature*, *398*(6729), 694–697.
Timmermann, A., J. Sachs, and O. E. Timm (2014), Assessing divergent SST behavior during the last 21 ka derived from alkenones and G. ruber-Mg/Ca in the equatorial Pacific, *Paleoceanography*, *29*, 680–696, doi:10.1002/2013PA002598.
Tingley, M. P., and P. Huybers (2010), A Bayesian algorithm for reconstructing climate anomalies in space and time. Part I: Development and applications to paleoclimate reconstruction problems, *J. Clim.*, *23*(10), 2759–2781.
Tudhope, A. W., C. P. Chilcott, M. T. McCulloch, E. R. Cook, J. Chappell, R. M. Ellam, D. W. Lea, J. M. Lough, and G. B. Shimmield (2001), Variability in the El Niño–Southern Oscillation through a glacial-interglacial cycle, *Science*, *291*(5508), 1511–1517.
Visser, K., R. Thunell, and L. Stott (2003), Magnitude and timing of temperature change in the Indo-Pacific warm pool during deglaciation, *Nature*, *421*(6919), 152–155.
Von Storch, H., and F. W. Zwiers (2001), *Statistical Analysis in Climate Research*, Cambridge Univ. Press, Cambridge, U. K.
Wang, Y. V., G. Leduc, M. Regenberg, N. Andersen, T. Larsen, T. Blanz, and R. R. Schneider (2013), Northern and Southern Hemisphere controls on seasonal sea surface temperatures in the Indian Ocean during the last deglaciation, *Paleoceanography*, *28*, 619–632, doi:10.1002/palo.20053.
Zebiak, S. E., and M. A. Cane (1987), A model El Niño–Southern Oscillation, *Mon. Weather Rev.*, *115*(10), 2262–2278.
Zhang, Z., M. E. Mann, and E. R. Cook (2004), Alternative methods of proxy-based climate field reconstruction: Application to summer drought over the conterminous United States back to AD 1700 from tree-ring data, *Holocene*, *14*(4), 502–516.
Zhao, M., C.-Y. Huang, C.-C. Wang, and G. Wei (2006), A millennial-scale u 37 kâĂš sea-surface temperature record from the South China Sea (8 N) over the last 150 kyr: Monsoon and sea-level influence, *Palaeogeogr. Palaeoclimatol. Palaeoecol.*, *236*(1), 39–55.
Zheng, W., P. Braconnot, E. Guilyardi, U. Merkel, and Y. Yu (2008), Enso at 6 ka and 21 ka from ocean-atmosphere coupled model simulations, *Clim. Dyn.*, *30*(7–8), 745–762.